Research Performance Final Report

Project Title:	Crosscutting Recombination Metrology for Expediting V_{OC} Engineering
Project Period:	08/01/16 – 07/31/19
Project Budget:	$1,025,000 (original) $952,757 (revised)
Submission Date:	10/16/19
Recipient:	Texas State University
Address:	601 University Drive San Marcos, TX 78666
Award Number:	DE-EE0007541
Project Team:	Texas State University National Cheng Kung University University of Toledo NREL
Principal Investigator:	Mark W. Holtz, Professor Phone: 512-245-2131 Email: mark.holtz@txstate.edu
Acknowledgment:	This material is based upon work supported by the Department of Energy under award number DE-EE0007541.
Disclaimer:	This report was prepared as an account of work sponsored by an agency of the United States Government. Neither the United States Government nor any agency thereof, nor any of their employees, makes any warranty, express or implied, or assumes any legal liability or responsibility for the accuracy, completeness, or usefulness of any information, apparatus, product, or process disclosed, or represents that its use would not infringe privately owned rights. Reference herein to any specific commercial product, process, or service by trade name, trademark, manufacturer, or otherwise does not necessarily constitute or imply its endorsement, recommendation, or favoring by the United States Government or any agency thereof. The views and opinions of authors expressed herein do not necessarily state or reflect those of the United States Government or any agency thereof.

Executive Summary

Work carried out under this grant addressed the need for improved materials and device characterization of solar cell designs. This experimental program aimed to develop joint electrical and optical studies of solar cells based on the group-II-VI semiconductor CdTe and the chalcogenide semiconductor $Cu(InGa)Se_2$. Electrical measurements focused on temperature (T) and illumination intensity (I) dependence of the open-circuit voltage (V_{OC}), a quantity that plays an important role in conversion efficiency. The V_{OC} depends on temperature and illumination intensity through the energy gap and positions of the quasi-Fermi levels (QFLs). Optical measurements exploited the illumination and temperature dependence of absolute photoluminescence (PL) intensity (PL-I), a quantity that also depends on the QFL positions. The QFL splitting is a quantity that also depends on recombination rates within the solar cell, including radiative and non-radiative processes. Other factors affect the electrical and optical properties. These include band offsets at both the front and back interfaces of the device active region where electrical contacts are formed. Understanding, locating, and quantifying the recombination properties of the solar cells was the principal goal of this research.

Custom simulations were developed to solve continuity and Poisson equations self-consistently to obtain free-electron and free-hole concentrations. The measurements of temperature and intensity dependent V_{OC} and PL-I allowed the extraction of a number of physical parameters including the conduction band offset, the shunt constant, and the effective capture coefficient for recombination centers, both within the absorber and at the absorber-buffer interface. In addition, the back-contact barrier height is determined from electrical properties. Each of these is discussed in the report.

The illumination intensity dependence of V_{OC} and PL-I do not overlap in experiments primarily because PL is not observed in the low-intensity regime where V_{OC} is studied. Absolute PL-I measurements enabled development of an approach directly comparing it with V_{OC}. This in turn allowed development of a simulation capability that would consistently use both measurements, as functions of T and I, for producing a minimization scheme using a differential evolution algorithm.

The approach was applied to both CdTe and $Cu(InGa)Se_2$ solar cells each prepared under various conditions. Shunt conductivity, QFL splitting, recombination were measured. Also extensively studied are current-voltage and frequency-dependent capacitance voltage.

Work completed under this grant included studies of magnesium zinc oxide (MZO) buffered CdTe solar cells including the effects of hydroiodic acid (HI) treatment. From these studies the recombination rates were quantified at the buffer/absorber (front) interface. The effect of back-contact barrier height was investigated. CdTe solar cells were prepared with CdSe and CdS buffer layers. Lower grain-boundary potential fluctuation, higher back-contact barrier height, and greater bulk recombination were observed in early devices with CdSe buffer layer.

Investigations were also carried out into $CdS/Cu(InGa)Se_2$ solar cells. A metal-insulator-semiconductor capacitance-voltage technique was developed to extract recombination-relevant properties of the absorber interface. From this work the density of interface states D_{it}, their capture cross-section σ, fixed charge at the interface Q_f, and surface recombination velocity were all extracted.

Table of Contents

Section Title	Page
Executive Summary	2
Background	3
Introduction	5
Project Results and Discussion	7
Conclusions	39
Budget and Schedule	41
Path Forward	41
Publications Resulting from This Work	42
Acknowlegments	44
References	44

Background

Recent articles have reported the use of initial PI Dr. Jian Li's approach [1, 2] to quantify the recombination rates in three distinct regions of $Cu(InGa)S_2$ (CIGS) based devices: *interface*, *space-charge*, and *bulk* (quasi neutral region).[3-9] Researchers from Solar Frontier K. K. used this approach to study the effect of alkali metal post-treatment and (Zn, Mg) O buffer layer on recombination rates of Cd free $Cu(In,Ga)(Se,S)_2$ minimodules.[4, 6, 7] The (Zn,Mg)O improves the transmittance of the window layer and reduces the interface recombination rate. The alkali metal post-treatment (K, Cs) showed increase in the free-carrier concentration, and reduced recombination rates throughout the whole absorber layer, which leads to better performance of solar cell devices. The key achievement of their study is obtaining efficiency ~ 20 % on minimodule having identical structure to the production modules. Similarly Kim *et al*. from National Institute of Advanced Industrial Science and Technology in Japan have studied the recombination rates in sulfurized and post deposition KF treated $Cu(InGa)Se_2$ thin-film solar cells.[9] Results suggest that the surfurization of surface created graded band gap at front side of $Cu(InGa)Se_2$ absorber with depletion of Ga. The graded absorber layer results into reduction of recombination rates at the buffer-absorber interface, space-charge, and bulk, which consequently improved the Voc and conversion efficiency of devices by a factor of 1.25. Further, the post deposition KF treatment of sulpurized samples also reduced the recombination rate in the bulk of absorber layer comparison to untreated samples. At National Renewal Energy Laboratory Guthrey *et al.* published an article which used the approach to study the effect of NaF and KF post deposition treatment on CIGS solar cells on soda-lime gkass and alkali-free sapphire.[8] The authors suggest that the benefit of alkali post deposition treatments depends on substrate. The interface recombination rate is reduced in devices grown on sapphire substrates whereas the recombination is reduced in the quasi-neutral regions of devices grown on the soda lime glasses.

The recent use of the recombination approach by independent groups demonstrates the effectiveness of this approach for pinpointing recombination losses in the three distinct regions of the devices. The recombination approach has the potential to act as 4th

generation metric or guiding strategy to improve the properties of solar cell devices. The demonstrated success of spatially quantifying recombination losses leads to the far more challenging problem which is to spatially quantify and types of recombination rates throughout the device. The original approach of Li's method includes mainly electrical analysis which include V_{OC} function of intensity and temperature to investigate the recombination rates. Quantifying the recombination rates throughout the device requires adding optical analysis in conjunction to the relatively well-established electrical analysis. The joint approach of electrical and optical analysis is first of its kind and has never been done before.

The goal of this project was to develop a metrology to achieve quantitative extraction of the spatially- and type-resolved recombination distribution with a unified electrical-optical analysis framework, a schematic diagram of which is shown in Figure 1. The methodology and instrumentation were conceived to advance the state-of-the-art using the 4th-level metric of recombination rate as a function of position, $R_j(x)$, with high spatial resolution and dynamic range. Experimental studies were carried out on solar cells based on CdTe and $Cu(InGa)Se_2$ (CIGS).

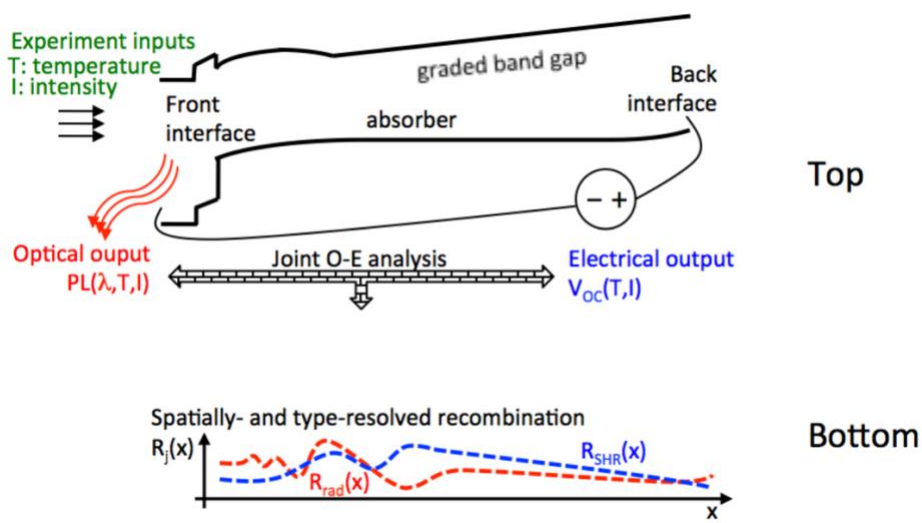

Figure 1. (Top) A schematic diagram showing the experimental inputs and outputs measured from a PV device with graded-bandgap absorber and the metrology to yield (Bottom) the 4th-level metric of spatially- and type-resolved recombination rates of $R_{SRH}(x)$ and $R_{rad}(x)$.

Unlike Si, thin-film PV has long needed advanced and reliable metrology to reliably link V_{OC} to materials synthesis. This is because recombination in thin-film PV is *spatially distributed and non-uniform*. The state of the art of recombination metrologies based on 3rd-level metrics – e.g., saturation current density J_0 and carrier lifetime τ – use a single lumped parameter which is inadequate for describing the complex recombination landscape in thin-film PV technologies. This project's goal is to develop the next-generation recombination metrology using the new 4th-level metric – spatially and type-resolved quantitative characterization of all pertinent types of recombination rates in PV devices. This metrology advances the state of the art by providing unprecedented power to PV researchers and manufacturers for V_{OC} improvement – the spatial resolution enabling pinpointed locations of problematic recombination and the type-resolution

guiding the strategy of materials and device engineering. The overall work scope is built around the critical path of first developing electrical-optical cross-calibration for an ideal scenario, then developing a practical but approximate version for rapid applications, then developing the exact-solution version for in-depth R&D applications, and finally optimizing and transferring the technology to industry.

The core of the approach is parallel electrical and optical measurements, both as a function of temperature (T) and illumination intensity (I). The originally planned measurements were V_{OC}(T,I) and photoluminescence spectroscopy PL(λ,T,I) using absolute PL intensities. While absolute PL spectroscopy was ultimately studied, in many cases it was found to be inconclusive since the excitation intensity range was narrow. Our approach was modified to rely, instead, on PL intensity measurements PL-I(λ,T,I) where the I in parentheses is illumination intensity. We subsequently carried out PL spectroscopy to supplement our other measurements.

Additional electrical properties were also motivated to better understand barriers and offsets within CdTe and CIGS solar cells. The measurements relied primarily on C-V studies as a function of temperature and drive-voltage frequency (f). The latter are known as admittance spectroscopy (AS) studies.

Two manuscripts capture the nearest outcome to joint electrical and optical measurements of solar cells to understand device-related properties. The first manuscript on CdTe-based devices was published in 2019. The second manuscript, on CIGSe solar cells, is under review. The majority of this report will be devoted to the CdTe publication.

We extract a set of solar cell parameters by focusing on a joint analysis of open-circuit voltage (V_{OC}) and photoluminescence intensity (PL-I) as a function of both temperature and illumination intensity. In general, V_{OC} is more sensitive to band offsets while PL-I is sensitive to overall recombination rate. Only a few studies have aimed to combine multiple measurement types.[10-13] The present approach differs from the others in several important ways. First, series resistance complications are avoided. Second, rather than revising a model for each additional measurement technique, to account for each new experimental feature qualitatively, the most suitable parameters are determined quantitatively by simultaneous least-square error fit to both the temperature- and excitation-dependent V_{OC} and PL-I data. To define a single mean square error between data and model for both V_{OC} and PL-I, the latter must be converted to units of eV. Therefore, the *absolute* PL intensity was measured. This allows determination of the quasi-Fermi level splitting between the electron and hole populations (ΔE_F) within the absorber from a calculation based on the Generalized Planck's Law. [14]

Introduction

Budget Period 1 (Year 1) of this research program articulated four major tasks aimed at developing the experimental capabilities and early forms of the analysis.

- Construct electrical and optical experimental setups.
- Develop metrology for the ideal scenario.
- Develop PL(λ,T,I) analysis, the approximate scenario.
- Develop V_{OC}(T,I) analysis, the approximate scenario.

During this period several samples were produced for the program by the University of Toledo and the National Renewable Energy Laboratory. These were, respectively, CdTe and $Cu(InGa)Se_2$ based solar cells. Initial forms of the experimental setups were produced and experimentation started. In this budget period two experimental issues were confronted. (1) The broadband illumination source for carrying out the joint analyses in a single apparatus did not have sufficient total intensity to produce PL from the samples provided or, indeed, any samples available including reference materials that produce good PL signals using laser illumination. We resolved this in two ways. One was to introduce a laser source with the system for carrying out the needed PL spectroscopy. Second was to configure and qualify a separate PL setup that was specifically designed for this type of measurement. (2) Literature on system calibration, for measuring absolute PL *intensity*, was inadequate. Conversations with others who have reported these measurements were not productive. Spanning this period and into the next, significant effort was invested in various scenarios for intensity calibration. Ultimately, *this was resolved* in budget period 2 and a descriptive article published to guide others who may wish to reproduce our result.

Also, during this period, the V_{OC} measurements were extensively developed and used to qualify the ideal and approximate analyses. A custom simulation program was developed utilizing Poisson's equation and excitation-dependent Fermi statistics to interpret the $V_{OC}(T,I)$ and $PL(\lambda,T,I)$ data as it became available. Also during this period we were confronted by low PL intensities that prohibited conducting spectroscopy studies across a broad excitation intensity range. *We resolved this challenge* by turning to PL Intensity measurements, PL-I(T,I), which collect the spectroscopically unresolved or integrated emission. This was ultimately understood to have intensity measurable across several orders of illumination intensity, but did not generally extend down to the range where $V_{OC}(T,I)$ was conducted.

As this budget period closed, the PI relocated overseas and a change of PI was executed.

Budget Period 2 (Year 2) of this research program articulated four major tasks aimed at integrating the experimental capabilities developed and the recombination analysis.

- Develop the $PL(\lambda,T,I)$ analysis, the exact-solution scenario.
- Develop the solution for Shockley-Read-Hall recombination of the exact scenario.
- Use the new metrology to guide improvement to CIGS baseline.
- Use the new metrology to guide improvement to CdTe baseline.

As mentioned above, $PL(\lambda,T,I)$ analysis was largely abandoned for the joint electrical and optical measurements due to low PL intensity. Work aimed at improving the simulation software was carried out for joint analysis of $V_{OC}(T,I)$ and $PL(\lambda,T,I)$ data. Spatial resolution was primarily addressed by determination of recombination properties related to interfaces versus "bulk" portions of the solar cells.

The joint electrical-optical measurements and analysis is the first of its kind in the PV community. It represents an important stride in the methodology development of PV characterization and device modeling. Because the $V_{OC}(T,I)$ and PL(T,I) data were taken at low and high intensities regimes, respectively, the experimental space for recombination probing is greatly expanded to allow a wider observation window for

previously unheeded mechanisms. At the same time, the overlap between the two intensity regimes assures self-consistency between the optical and electrical domains. The resultant benefits include new detection sensitivity and quantitative resolution of importance mechanisms such as shunting and band offset. The fact that this project developed home-grown numerical tool for the simultaneous electrical-optical analysis also means the potential of rapid desemination to industrial parteners in the PV community.

As this budget period closed, shortfalls in the spatial resolution of the method developed to this point and the impact of those shortfalls on feedback to baseline devices resulted in a restructuring of the grant and subsequent tasks.

Budget Period 3 (Year 3) of this research program originally articulated four major tasks that were ultimately reduced to a single task:

- Conduct measurements and write manuscripts according to revised statement of work (SOW).

Seven manuscripts were articulated in this revised SOW for publication in peer-reviewed journals. (This accounting does not include conference papers.) As of the writing of this report, four of these have been published, one is under review, and two others are at various stages of revision by the authors. These complement the six manuscripts (total) published in 2017 and 2018 under this award.

Citations to the peer-reviewed publications in print are included in the reference section.[14-24]

Project Results and Discussion

Section 1: Joint electrical and optical analysis for determination of parameters affecting CdTe solar cell performance

"Measurement of band offsets and shunt resistance in CdTe solar cells through temperature and intensity dependence of open circuit voltage and photoluminescence" (Solar Energy https://doi.org/10.1016/j.solener.2019.07.057).

This study has the goal of extracting a set of solar cell parameters from joint electrical and optical measurements. In addition to the V_{OC} and PL-I, we adopt the value of Φ_b from the rollover method on the current-voltage-temperature (JVT) curves.[25] Only a few studies have aimed to combine multiple measurement types.[10-13] *The effort presented here differs from these others in several important ways.* First, series resistance complications are avoided, since although the rollover portion of the JV curve is in the forward current region, the rollover method should be robust against the effects of varying series resistance.[26] Second, rather than revising a model for each measurement technique to account for each new experimental feature qualitatively, the most suitable parameters are determined *quantitatively* by arriving at the least square error fit to the temperature- and excitation-dependent V_{OC} data, and simultaneously to the PL-I data. To define a single rms difference between data and model for both open circuit voltage and PL-I, the PL-I data must be converted to units of eV. Therefore, the *absolute* PL intensity was measured, and the quasi-Fermi level splitting between the electron and hole

populations (ΔE_F) within the absorber was extracted from a calculation based on the Generalized Planck's Law. [14]

Ohmic back contacts have been an elusive achievement in CdTe-based solar cells. The back-contact barrier, Φ_b, is a challenge for standard characterization methods and for further improving photovoltaic performance. The back-contact barrier decreases the fill factor and open circuit voltage (V_{OC}) in complicated ways,[27] and distorts capacitance-voltage (C-V) measurements of the doping concentration.[28] When measuring trapping center properties by AS, trap signatures can be altered by the presence of Φ_b [29] and apparent signatures can be wholly produced.[30] It has been questioned whether Φ_b may render AS unusable for its original purpose of characterizing deep centers.[31] Reducing Φ_b is desirable for the back contact. While metals with deep work functions are more likely to be successful for contact to *p*-type materials, other factors at the back interface have considerable influence. For example, it has been found that a Te-rich back surface tends to result in improved performance. It is possible that a thin layer with a favorable conduction band offset from CdTe may be formed from Cu-Te compounds,[32, 33] and that such a layer would have an electron blocking effect. Alternatively, the Te may form an intermediate band offset between the absorber and back contact.[34] Another possible mechanism is that the Te may block Cu from diffusing into the CdTe absorber and reaching the front buffer layer,[35] where excessive Cu becomes deleterious.[36]

Other factors at the back contact include the use of interlayers in an attempt to lessen the shunt conductance (G_{SH}) between the front and back electrodes.[37, 38] Even without a true pinhole contact, any sufficiently thin region within the absorber can exhibit space-charge-limited current (SCLC), where the conductance is approximately proportional to voltage V with a proportionality constant K, or $G_{SH} \approx K\,V$.[39]

Figure 2 shows the band offsets that affect solar cell performance. A 4-μm thick *p*-CdTe absorber layer is depicted with a band gap of E_G = 1.5 eV and a 90-nm thick buffer of CdS having a band gap of E_{GW} = 2.5 eV. The front absorber-buffer junction conduction band offset (ΔE_C), and the (hole-blocking) front valence band offset can be expressed in terms of ΔE_C and the band gaps as shown. The barrier height of the main junction is Φ_f.

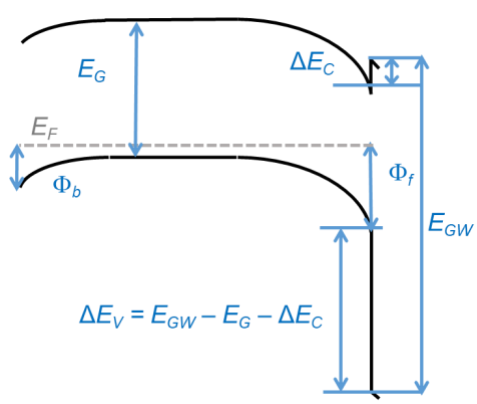

Figure 2. Band offsets that may affect solar cell performance. A 4-μm thick p-type absorber layer is depicted with a band gap of E_G = 1.5 eV and a 90-nm thick buffer having a band gap of E_{GW} = 2.5 eV.

We examine a number of interlayers deposited at the back contact-absorber interface for improving the back-contact properties of the solar cells. To correlate device properties such as band offsets and shunt with experimentally obtainable characteristics, we employ a measurement and analysis technique coupling the temperature and excitation dependence of V_{OC} and photoluminescence intensity (PL-I) with custom numerical simulation studies of the device properties.

A large number of methods exist for correlating device properties to experimental current-voltage (JV) results.[40-42] These techniques are limited in their ability to provide physical insight, since, *e.g.*, the proportion of interfacial versus bulk recombination has no clear relationship with the contribution of each diode in a two-diode lumped-parameter circuit model. The existence of a back-contact band offset is not generally considered in these models.

Temperature-dependent V_{OC}, or V_{OC}(T,I), has been recently developed to probe recombination characteristics [2] while avoiding the complexities of series resistance.[43, 44] The V_{OC} versus temperature relationship near room temperature is extrapolated to absolute zero. The extrapolated voltage value (qE_a) can be correlated with the location of recombination within the device. More recently, it has been found that the value of qE_a can change with excitation, and this may be affected by front junction band offsets.[15]

We explore various back interlayers and front window layers. The analysis shows that some interlayers were successful at reducing shunt conductance, but an interlayer was not found which reduced the barrier height without an accompanying increase in shunt resistance. The analysis also provided a way of obtaining the front window conduction band offset.

Sample Description: Superstrate structures were fabricated beginning with three sequences of front buffer layers. The first sequence began with 2.3 mm thick AF45 borosilicate glass coated with bilayers of fluorine-doped tin oxide SnO_2:F (FTO) with 500nm thickness and undoped SnO_2 (TO) with 100 nm thickness, grown at the National Renewable Energy Laboratory (NREL) in a low pressure chemical vapor deposition system at 550˚C. Tetramethytin (TMT) was the tin precursor and bromotrifluoromethane was the F dopant source in an oxygen-rich ambient. Then, CdS:O with a thickness of 80 nm was deposited by magnetron sputtering, in a 6% O_2 in Ar ambient at 5 mTorr deposition pressure without heating. This window will be labeled CdS:O_6. CdTe was deposited by close space sublimation (CSS) at 600 °C, at 16 Torr in a 6.25% O_2 in He ambient. A $CdCl_2$ activation anneal was performed at 400 °C in dry air, followed by rinsing in methanol and drying with N_2 gas to remove extra $CdCl_2$ from the surface.

A blade-coated layer of CdTe nanoparticles (NP) in a pyridine solution was then added to reduce surface roughness, eliminate pinholes, and allow for the deposition of interlayers. (Details to be published later by S. Rab, *et. al.*) A second $CdCl_2$ activation anneal was carried out for the added NP material by dipping the samples into a solution of $CdCl_2$ in methanol with ~15 mg/mL concentration, heated at 60 ℃ for 15 s, rinsed with isopropanol, dried with a stream of N_2, placed on a 350 °C Al block for 20 s, then placed onto an Al block at room temperature for rapid cooling. Back contact Cu doping was done by submerging in a dilute 0.1mM solution of $CuCl_2$ and DI water for 2 min followed by rinsing in DI water and drying with N_2, followed by a 225 °C, 30 min anneal, then 150 °C

for 1 hour. Various interlayers were grown on devices with NP. Spin-coated Spiro-MeOTAD (2,2′,7,7′-tetrakis(N,N-di-p-methoxyphenylamino)-9,9′-spirobifluorene) and EH44 (2,7-Di(N,N-dimethoxyphenylamino)-N-(2-ethylhexyl)carbazole) are organic hole transport materials used in perovskite solar cells. Evaporated selenium and sputter coated indium tin oxide (ITO) are known to have deep work functions, particularly ITO with Cl and Au, which is often used to accomplish the formation of Ohmic contacts to *p*-type materials. SnTe interlayers and PbTe interlayers were grown by molecular beam epitaxy to a thickness of 250 nm and doped with Tl to a high *p*-type concentration of 10^{19} cm^{-3} to mitigate the back contact barrier. Finally, a 100 nm thick Au layer was deposited by thermal evaporation, forming 0.25 cm^2 area devices.

A second window sequence, grown at the University of Toledo, began with 3.2 mm thick TEC-15M commercial substrates, which consist of soda lime glass coated with SiO_2 to prevent sodium migration, then FTO with 500nm thickness and undoped TO with 100nm thickness. CdS:O was deposited by sputtering to a thickness of 80 nm with 1% O_2 in Ar ambient at 10 mTorr deposition pressure at 270 °C. This CdS:O_1 window layer was followed by CdTe grown by CSS at 660 °C, 50 Torr He ambient. A $CdCl_2$ activation anneal was performed at 400 °C in dry air, followed by rinsing in methanol and drying with N_2 gas to remove extra $CdCl_2$ from the surface. Cu doping was achieved by the evaporation of ~ 3 nm of Cu and 40 nm of Au, forming 0.09 cm^2 area devices, followed by a 30 min anneal at 200 °C.

A third window sequence was grown at the University of Toledo on 3.2 mm thick TEC-15M substrates. MgZnO (MZO) was deposited by sputtering without heating at 6 mTorr pressure. CdTe on this layer was grown by CSS at 560 °C. A $CdCl_2$ activation anneal was performed at 400 °C in dry air, with the exception of a final MgZnO device where it took place at 420 °C in an O-free ambient (He gas). The $CdCl_2$ activation step was followed by rinsing in methanol and drying with N_2 gas to remove extra $CdCl_2$ from the surface. Back contact Cu doping was done by submerging in a dilute solution of $CuCl_2$ and DI water for 2 min followed by rinsing in DI water and drying with N_2, followed by a 225 °C, 30 min anneal. Finally, a 40 nm thick Au layer was deposited by thermal evaporation, forming 0.09 cm^2 area devices.

Characterization: To measure power conversion efficiency (PCE) at room temperature, a class A solar simulator lamp was used. To measure temperature- and excitation-dependent open-circuit voltage, illumination was provided by a spectrally uniform laser-driven light source filtered from 400 to 850 nm, focused with achromatic lenses, controlled by neutral density filters, and measured with a power meter. Knowing the spectra for the power meter response, the source, and the filters allows us to convert measured power meter current to photons cm^{-2} s^{-1}. Since AM1.5 illumination gives a flux of 1.7×10^{17} photons cm^{-2} s^{-1}, with energy greater than the 1.5 eV band gap of CdTe, that flux was considered 1 sun equivalent. The current-voltage-temperature-intensity (JVTI) measurements were performed with this illumination inside of a helium closed-cycle cryogenic system at Texas State University using a Keysight B2912A source measure unit. AC measurements were made with a Keysight E4990A impedance analyzer. For C-V, DC bias was varied from -1.0 to 0.7 V. For AS, the frequency sweep was additionally varied from 1 kHz to 1 MHz and the AC modulation amplitude was 35 mV_{rms}.

For PL-I(T,I) the devices were illuminated with a 660 nm diode laser focused by a 6.5× objective lens into a microscopy cryostat. The spot diameter was found to be 120 μm using the knife edge method on a cleaved wafer. The laser power, controlled by neutral density filters, was measured with a NIST-traceable power meter to obtain the intensity. The superstrate solar cell devices were illuminated through the glass, which had a thickness of d = 2.3 or 3.2 mm. Therefore, after the cleaved wafer was removed, the focus point was lowered to the floor of the stage where the active device would rest, then also raised by $(1/1 - 1/n_g)d$ to account for the altered focus point of the laser light, where n_g = 1.5 is the index of refraction of the glass.

The resulting PL was collected through the same objective and passed through filters to remove the laser light. The PL intensity was recorded by a photomultiplier (PMT) attached to a lock-in amplifier with the laser chopped at 400 Hz. The laser intensity could be changed by a series of calibrated neutral density filters. To relate the number of photons to a raw detector signal, we measured the signal from an excitation laser spot on a Spectralon reflectance standard. [14] *This approach was developed under this award and is mentioned below.*

Studies were conducted and analyzed varying the temperature from 200 to 350 K, since the properties below 200 K can be dominated by more detailed effects such as carrier freeze-out, band gap temperature dependence, and inhomogeneous barrier heights.[45] V_{OC} was analyzed up to 350 K to ensure resolution of its temperature dependence near room temperature. [2] The excitation range for PL-I was chosen to be high enough for all samples to have a strong signal-to-noise ratio and yet low enough for laser spot heating effects to be minor. [18] *Establishing an approach to avoid laser heating during measurements was carried out under this award and is mentioned below.*

Data Analysis: The measurement of JVTI allowed the determination of Φ_b through the rollover effect.[25] The measurements of temperature and intensity dependent V_{OC} and PL-I allowed the extraction of a number of physical parameters: the conduction band offset ΔE_C, the SCLC shunt constant $K = G_{SH}/V$, and the effective capture coefficient for recombination centers, both within the absorber $c_a = N_{ta}\sigma_a v_{th}$ and at the absorber-buffer interface $c_s = N_{ts}\sigma_s v_{th}$, where N_{ta} is the density of recombination centers, N_{ts} is the sheet density of recombination centers at the interface, σ is the respective capture cross section, and v_{th} is the carrier thermal velocity. c_a is also the reciprocal of the minimum lifetime for a carrier type which could be caused by the absorber's recombination center, and c_s is also the maximum recombination velocity which could be caused by the interface recombination center. *Determination of recombination rates was a key component of the funded proposal.*

Mobilities, effective masses, and permittivity ε were taken from the commonly used baseline.[46] The absorber doping density was $p = 1\times10^{14}$ cm^{-3} from C-V measurements. Within the heavily doped SnO_2:F front contact, the E_F is 3.8 eV above its valence band.[47] Given a 2.7 eV valence band offset between CdTe and SnO_2,[48] the front contact barrier height (Φ_f) was therefore taken as 1.1 eV.

Since injection-dependent measurements are being considered, we cannot assume low injection or a constant minority carrier lifetime, particularly with such low doping. We will

however make the common simplifying assumptions that dominant recombination states must be within the mid-gap energy range and that the capture cross sections for electrons and holes are equal. In this case the recombination rate at a given location, where the electron concentration is n and the hole concentration is p, becomes $R = c_{a,s}\, np/(n+p)$. Each parameter set yielded the quantities V_{OC} and ΔE_F through a numerical model solving the continuity and Poisson's equations.[49] The parameter set was adjusted to find the minimum square difference fit to the temperature- and excitation-dependent V_{OC} and PL-I data simultaneously, using a differential evolution algorithm.[50]

Joint Electrical and Optical Measurements: The representative effects of each experimental variable has on V_{OC} are shown in Figure 3. The data are from what will be called the Control sample, listed first in Table I. The V_{OC} is typically greatest at low temperatures and high intensities where it is limited by the difference in the built-in voltages of the front and back junctions.[51, 52] In Figure 3 (a), the simulated effect of increasing non-radiative recombination in the absorber material (c_a) is shown, illustrating the uncertainty in the c_a parameter as fit to the measured voltages. The increasing slope of open circuit voltage with temperature (dV_{OC}/dT) is consistent with an increasing activation energy qE_a. The activation energy method of evaluating recombination associates a higher qE_a with more dominant bulk recombination, and so there is a qualitative agreement with the method presented here.[1, 2] In Figure 3 (b) an increased shunt causes the low intensity V_{OC} to drop, though shunting is less important at high intensity.[53] Figure 3 (c) replots the lowest intensity points in Figure 3 (a) in 2D for clarity.

In Figure 4 (a), also from the Control sample, non-radiative recombination is shown to cause a drop in the PL intensity as well. Meanwhile, the PL-I corresponding to shunting in Figure 4 (b) is unaffected, since it is taken experimentally at a high intensity where shunting is less important.

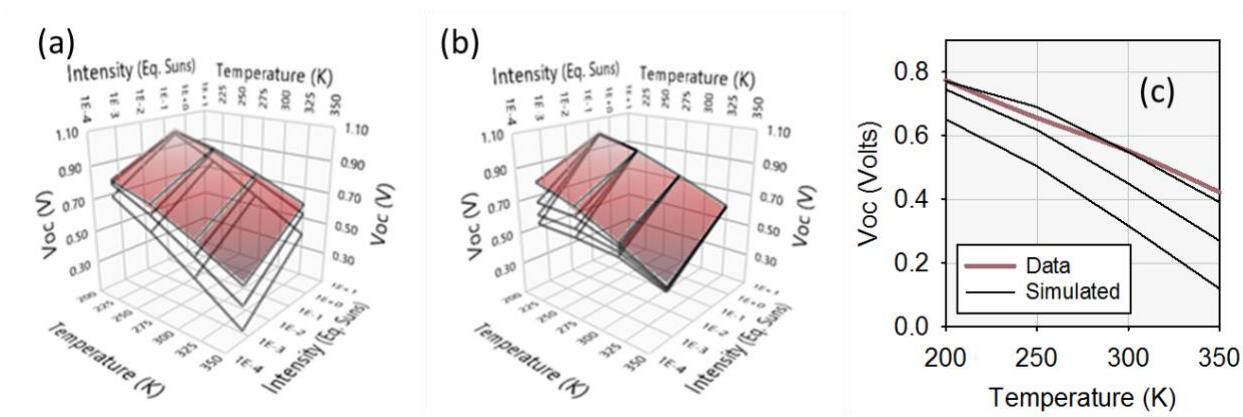

Figure 3. V_{OC} versus temperature and excitation intensity for the Control sample. V_{OC} data is shown as a surface, and the grids are simulated V_{OC} values, with parameters varying as: (a) c_a is increased from 1.3 to 13 to 130 $\times 10^7$ s^{-1}, and as (b) the shunting constant K is increased from 4 to 6 to 8 to 10 $\times 10^5$ $(\Omega\text{-V-cm}^2)^{-1}$. Each parameter increase for both c_a and K corresponds to a grid with a lower V_{OC}. (c) Shows for clarity a cross section view of the lowest intensity points in (a).

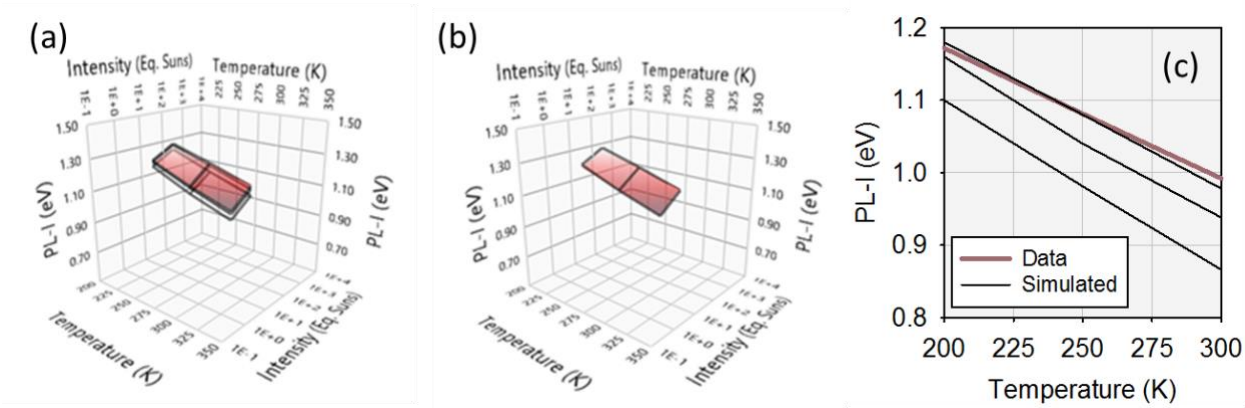

Figure 4. PL-I converted to ΔE_F versus temperature and excitation intensity for the Control sample. Experimental PL-I data is drawn as a surface, and the grids are simulated PL-I values, with parameters varying as: (a) c_a is increased from 1.3 to 13 to 130 $\times 10^7$ s^{-1}, and as (b) the shunting constant K is increased from 4 to 6 to 8 to 10 $\times 10^5$ $(\Omega\ V\ cm^2)^{-1}$. Each parameter increase (for both c_a and K) corresponds to a grid with a lower PL-I. (c) Shows a cross section view of the lowest intensity points in (a).

Along with recombination within the absorber, interfacial recombination may be significant, and it is known to be compounded by a negative or cliff-like ΔE_C. This is because such an offset can position a high *n*-type concentration in the buffer layer in close proximity to a high *p*-type concentration at the front edge of the absorber.[54] Additionally, ΔE_C can directly affect the electrical properties, even without considering interfacial recombination.[55]

A cliff-like $\Delta E_C < 0$ in the control sample had a weak effect on V_{OC}. This is because the interfacial recombination coefficient c_s turned out to be fairly small. For illustration purposes, the result of a -0.1 eV cliff-like step in ΔE_C is shown in Figure 5 (a) with an inflated c_s (essentially an infinite surface recombination velocity at the CdTe-window interface) to make the effects of cliff-like offset more visible. In this case, the slope of V_{OC} with temperature remains gentle with increasing interfacial recombination, in contrast to the case of increasing bulk recombination seen in Figure 3 (a). This is again consistent with the method of evaluating recombination mechanisms by slopes, which associates a high intercept of the room temperature V_{OC} slope, in the zero-temperature limit, with dominant bulk recombination.[1, 2]

A spike-like $\Delta E_C > 0$ results in an anomalous temperature peak of the V_{OC}, as in Figure 5 (b). This spike-related maximum in the V_{OC} [56] is more pronounced at high illumination, appearing between 250 and 300 K. The maximum can interfere with the standard method of probing recombination by finding qE_a from room temperature V_{OC}. Here, it is being used to evaluate absorber-buffer band offsets by fitting ΔE_C to the V_{OC} data.

Several quantities have overlapping effects on V_{OC}; for example the increased interfacial recombination shown in Figure 5 (a) is most effective at suppressing the low temperature, low intensity V_{OC}. This is similar to the primary effect of shunt resistance shown in Figure 3 (b). Therefore, these two parameters can become difficult to resolve, particularly when other effects are present.

The joint analysis with PL-I helps resolve ambiguity. Comparing Figure 6 (a) to Figure 4 (b), we see that the interfacial recombination has a deleterious effect on PL intensity while shunting has no effect. Requiring agreement of the model outputs to both Voc and PL-I data distinguishes these cases. In general, Voc is controlled by both the rate of recombination and by band offsets, but the intensity of PL tends to be sensitive to recombination, not band offsets.[57]

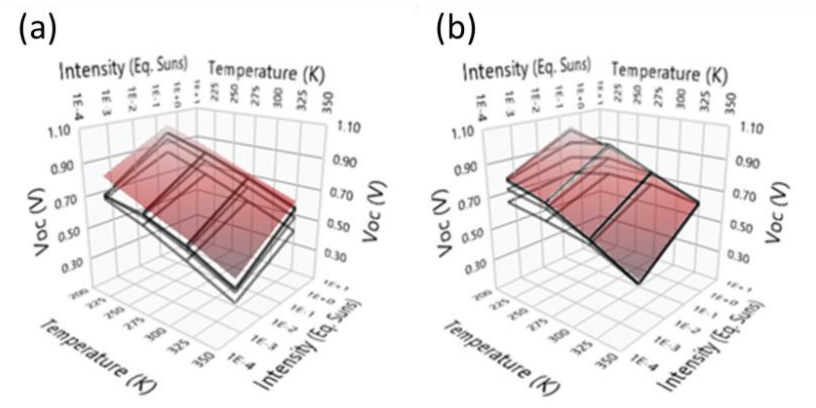

Figure 5. Voc versus temperature and excitation intensity for the Control sample. Voc data is drawn as a surface, and the grids are simulated Voc values, with parameters varying as: (a) ΔE_C is changed from 0 to -0.1 to -0.2 to -0.3 eV, making it more cliff-like. Also, c_s was inflated by a factor of 10,000x in these simulations, which is essentially setting an infinite recombination velocity at the interface. (b) ΔE_C is changed from 0 to +0.1 to +0.2 to +0.3 eV, making it more spike-like. Each parameter step (for both c_s and ΔE_C) corresponds to a grid with a lower Voc.

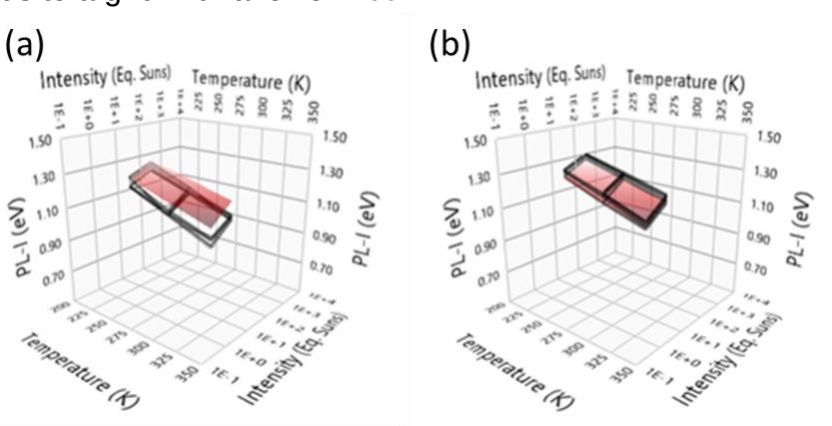

Figure 6. PL-I versus temperature and excitation intensity. Experimental PL-I data is drawn as a surface, and the grids are simulated PL-I values, with parameters varying as: (a) ΔE_C is changed from 0 to -0.1 to -0.2 to -0.3 eV, making it more cliff-like. Also, c_s was inflated by a factor of 10,000x in these simulations, which is essentially setting an infinite recombination velocity at the interface. (b) ΔE_C is changed from 0 to +0.1 to +0.2 to +0.3 eV, making it more spike-like. Each parameter step (for both c_s and ΔE_C) corresponds to a grid with a lower PL-I.

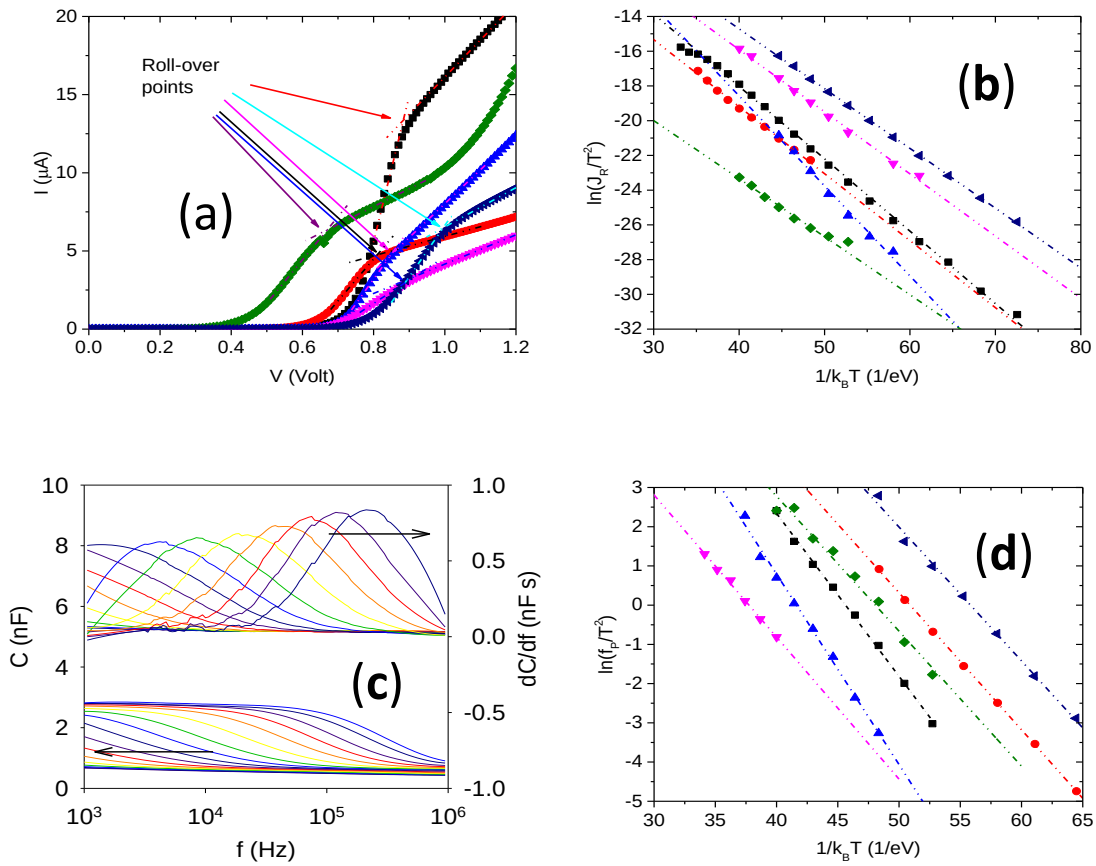

Figure 7. Comparison of JV-based and capacitance-based methods for measuring back contact offset. Results from the CdS:O_6 samples in Table 1 are shown for illustration. (a) The current of the roll-over point of a JV curve, here shown at 190K, was found as a function of temperature and placed on (b) an Arrhenius plot whose slope provides the barrier height energy. (c) The frequency of the inflection point of an admittance curve was found as a function of temperature and placed on (d) an Arrhenius plot whose slope provides the AS value of barrier height energy.

Results used to extract Φ_b are shown in Figure 7. In all cases, the Φ_b from the JVT rollover effect was 1.1-1.3 times the value from AS, as expected from previous reports.[30] The parameters can be seen in Table 1, along with Φ_b and the PCE under AM1.5 solar illumination. The first device on the list is considered the Control sample. A dozen devices were made with the blade-coated CdTe nanoparticle (NP) layer and a dozen without. NP was found to assist in reproducibility, with the best non-NP devices equivalent to the Control device.

Decreasing the deposition oxygen ratio of CdS:O from 6% to 1% resulted in a more cliff-like ΔE_C (< 0), as might be expected from a decrease in band gap.[58] Although, other studies involving a more drastic lowering of oxygen content have suggested that it could instead increase the band gap by decreasing S-Te diffusion.[59] The complete substitution of the CdS:O (and undoped SnO_2) buffer with a MgZnO buffer causes a

strongly spike-like offset (ΔE_C > 0). This is clear from Figure 8, which develops the same temperature peak seen in Figure 5 (b).

The bulk recombination coefficient c_a varied from 1-5×10^7 s^{-1}, with the exception of the final MgZnO device where the $CdCl_2$ activation step took place in an O-free ambient (He gas). The PCE increased from 14 to 15%, and this was attributed to a reduced c_a = 5×10^6 s^{-1}.

The interfacial recombination coefficient c_s varied from 10^4 to 10^6 cm s^{-1}. Measurements were sensitive to the value of c_s primarily for the two CdS:O_1 samples (3×10^5 cm s^{-1}) as these had a cliff-like ΔE_C, making the interface a dominant source of recombination. Thus, this analysis allows the detection of the band alignment as the reason for MZO's success as a front interface contact. In comparison to CdS:O the surface recombination velocity is unimproved or even inferior.

Table 1. Fitting results, with power conversion efficiency, rollover-based barrier height, and slope of the JV curve at the short circuit point.

Device structure starting with glass/SnO_2:F/	PCE	ΔEc	c_a	c_s	Φ_b	K	dJ/dV
	%	eV	10^7 s^{-1}	10^5 cm/s	eV	10^{-5} (Ω V cm^2)$^{-1}$	10^{-5} (Ω cm^2)$^{-1}$
SnO_2/CdS:O_6/CdTe/NP/Au	16	0.01	1.3	0.3	0.38	4.3	29
SnO_2/CdS:O_6/CdTe/NP/ITO/Au	14.7	-0.01	1.3	0.5	0.45	1.0	38
SnO_2/CdS:O_6/CdTe/NP/Se/Au	15.6	0.04	3.4	0.3	0.36	6.0	86
SnO_2/CdS:O_6/CdTe/NP/SnTe/Au	13.5	0.05	1.5	0.1	0.59	0.8	21
SnO_2/CdS:O_6/CdTe/NP/Spiro/Au	10.9	0.07	5.7	1.0	0.4	5.3	130
SnO_2/CdS:O_6/CdTe/NP/EH44/Au	15	0.01	2.0	0.2	0.38	5.5	100
SnO_2/CdS:O_1/CdTe/Au	13	-0.16	4.7	2.9	0.45	4.1	74
SnO_2/CdS:O_1/CdTe/HI etch/Au	15	-0.18	2.4	3.8	0.35	4.1	46
MgZnO/CdTe/Au	14	0.20	2.5	11	0.38	0.1	100
MgZnO/CdTe/O-free activ./Au	15	0.22	0.5	8.0	0.38	0.1	110

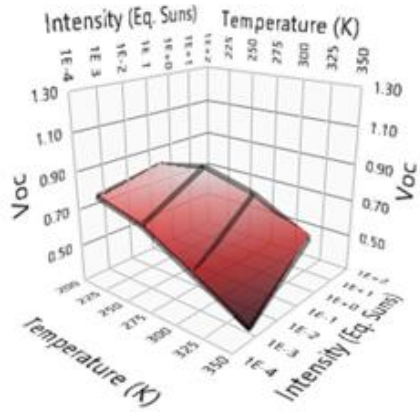

Figure 8. V_{OC} data (surface) and simulated (mesh) for the MgZnO/CdTe/oxygen-free activated/Au device, illustrating the existence of a spike-like absorber-buffer conduction band offset.

The back-contact interlayers did not produce a major reduction of Φ_b, though a hydroiodic (HI) acid etch had reduced the barrier by 0.1 eV below an untreated back surface. What variation in Φ_b the interlayers caused did not correlate to changes in PCE. In the case of a Se interlayer, for example, the barrier was slightly decreased while the efficiency fell. One interpretation relies on problems in specifying the measured Φ_b due to inhomogeneous back contact barrier. That is, certain regions of each back contact might have a lower or higher Φ_b due to local variations in composition. The effective barrier of Φ_b^* would then be dominated by the lower barrier regions, leading to a temperature-dependent value of $\Phi_b^* \approx \Phi_b - s^2/(2\, k_B T)$ where s is the standard deviation of the barrier height.[60, 61] The same interpretation was previously suggested when it was found that the amount of *p*-type doping from Cu incorporation was unable to explain the beneficial effect of Cu on the back surface.[62]

Rollover measurements were made in the range 180 K to 280 K. Thus, for the measured rollover Φ_b to differ appreciably from the room temperature Φ_b, the standard deviation s would need to be very large, yet there is no evidence of a strong quadratic dependence of rollover on reciprocal temperature, nor do previous estimates show a drastic change in Φ_b at such a temperature range in CdTe devices.[45]

Another cause of PCE variation would be shunting at the front junction. One standard method of estimating shunt conductance is from the derivative dJ / dV at the short circuit (zero voltage) point.[63, 64] However, the apparent shunt found from a JV curve is distorted by voltage-dependent collection current and also by the band offsets in heterojunction solar cells. Even when ignoring the effects of Φ_b, this derivative can have an extremely strong dependence on the value of the front band offset ΔE_C.[65] The V_{OC}-T-I and PL-I-T technique allows an estimation of physical shunting conductance, rather than the lumped parameter of dJ/dV. Since a device's normal operating range is ~0.9 Volts, the SCLC shunt conductance constant K in (Ω V $cm^2)^{-1}$ may be compared directly to the slope in (Ω $cm^2)^{-1}$ shown Table 1, and the shunting is found be an order of magnitude weaker than the slope method would suggest. Most strikingly, the MZO

windows yield the worst apparent shunt (d*J*/d*V*) yet the best shunt from the fitted VOC-T-I & PL-I-T data.

That the slope method gives an inaccurate value is clear from the low intensity V_{OC}, where the device is simply not being provided with enough photocurrent to account for an Ohmic shunt of conductance d*J*/d*V*. This suggests that the many reported estimations of shunting by the standard slope method largely do not represent a physically meaningful shunting path in heterojunction solar cells. Shunt resistances estimated by the slope method must not be taken as representing a physical shunting connection unless they are far below 1 kΩ-cm^2.

One result which does not appear in Table 1 is that of the PbTe:Tl interlayered device. This device was unusual because there is no rollover, and hence no evidence of Φ_b in the JV curve depicted in Figure 2. We include the Control device, for direct comparison, which shows the rollover near 1 V. Moreover, the PbTe:Tl device's C-V results, shown in Figure 10 as a Mott plot, $N_{CV} = (2/q\varepsilon)/[d(C^{-2})/dV]$, do not show the U-shape expected for structures with a back contact barrier,[66] as seen on the Control sample C-V result which is representative of all of the other devices.

It is possible that the lack of a U-shaped C-V result could be related to a Cu diffusion effect seen in previously reported C-V results that were similar in appearance and depth.[67, 68] In the present case, the Cu was already deposited and diffused before the PbTe interlayer, and even the sample with a SnTe interlayer did not exhibit these effects despite undergoing a close to identical process. The time-resolved photoluminescence (TRPL) lifetime was the highest for the PbTe device as well. All of these suggest that PbTe:Tl is forming an excellent Ohmic contact.

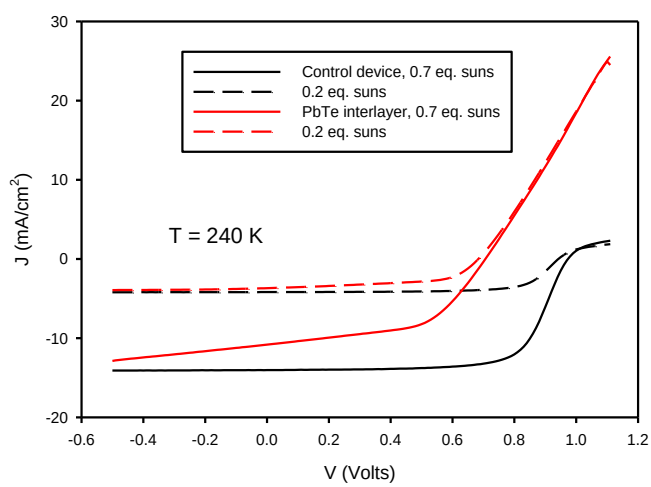

Figure 9. Comparison of typical JV curves the with those from the PbTe:Tl back contact interlayer device.

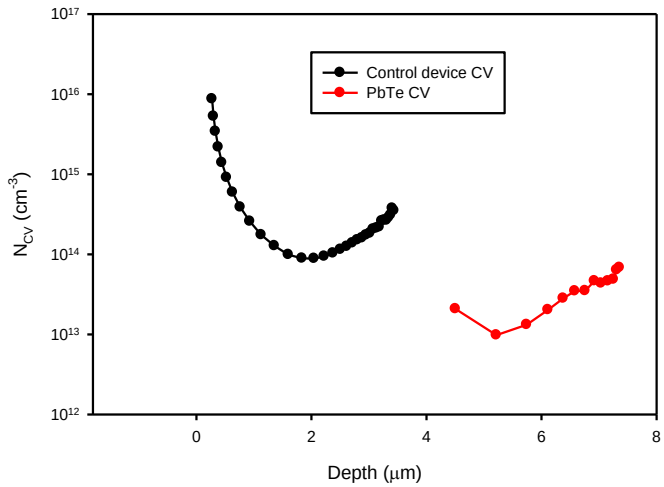

Figure 10. Room temperature comparison of typical C-V effective doping concentration curves with those of the PbTe:Tl back contact interlayer device.

However, this device has the lowest efficiency of all (9%) with a V_{OC} that does not rise above 700 mV. We believe that there is an additional presence of a strong photoconducting shunt, caused by the PbTe interlayer. The effect can be seen on the more strongly illuminated JV curves in Figure 9. While the slope method is not normally quantitative, the overall linear form of the JV curve suggests a very high shunt of 200 Ω cm^2, but only when illuminated. It appears that the interface between PbTe and CdTe is undergoes complicated changes in band bending with light, which is not unexpected from previous studies of strong band-bending and persistent photoconductivity when these materials are grown together in single crystal form.[14, 69] A separate report on PbTe results will be published that is outside of the scope of this award.

Summary: The back-contact barrier and the front buffer conduction band offset present special challenges for heterojunction solar cells such as those based on CdTe. These factors impact cell performance and characterization methods are still unsettled. Further, they compound the difficulty of characterizing more conventional obstacles such as recombination centers and shunting. V_{OC}(T,I) provides new insight, associating clear, measurable features with the desired offsets and shunts. When complemented with PL(T,I), signatures of band offsets that are otherwise difficult to distinguish from recombination effects become more resolvable. *When combined with numerical simulation, the recombination characteristics, offsets, and shunts can be obtained quantitatively.*

ITO and SnTe:Tl interlayers were successful at reducing shunt, but the barrier height did not show the hoped-for reduction. The other interlayers attempted did not significantly reduce the shunt or barrier, though HI etching reduced the back-barrier height by 0.1 eV in CdS:O- samples suggesting that a direct reduction in Φ_b, rather than a Cu diffusion reduction mechanism, is responsible for the improved performance of a Te-rich surface. Heavily Tl doped PbTe appeared to reduce or eliminate the barrier height, yet it was marred by strongly photoconducting shunt. This suggests a possibility that *p*-PbTe, in

combination with another interlayer, may eliminate the shunt effect while lowering the barrier.

The doping of CdS with oxygen to widen the band gap appears to have effect of raising its conduction band with respect to CdTe, yielding a less cliff-like offset. The increasingly popular MgZnO (MZO) front buffer has a large spike-like offset which effectively reduces interfacial recombination without reducing recombination velocity, and tuning the Mg/Zn ratio to obtain a reduction in gap of 0.1 eV may prove beneficial to future architectures.

Section 2: Joint electrical and optical analysis for determination of parameters affecting CIGSe solar cell performance

We now turn our attention to the results of joint electrical and optical studies of CIGSe solar cells. This work is currently under review.

"Measurement of shunt resistance and conduction band offset in $CuIn_{1-x}Ga_xSe_2$ solar cells through joint analysis of temperature and intensity dependence of open-circuit voltage and photoluminescence" (under review)

$Cu(In,Ga)Se_2$ (CIGSe) solar cells are a successful industrial-scale thin-film technology with which high efficiencies have been achieved. Room for improvement remains in increasing open-circuit voltage (V_{OC}) and in closing the fairly wide gap between the best cells at over 23% efficiency [70] and a typical 14% module product efficiency.[71] Devices made with a variety of properties and fabrication processes often yield similar efficiencies, and further optimization depends on separating the effects of parasitic resistances, band offsets, and recombination.[72] A band diagram defining the relevant energies is shown in Figure 11. Separating these mechanisms is complicated by the interdependent effects of multiple physical parameters on any particular measurement. For example, the apparent parasitic shunt resistance found from a current-voltage (JV) curve is very distorted in heterojunction solar cells by the presence of a front conduction band offset (ΔE_C).[13]

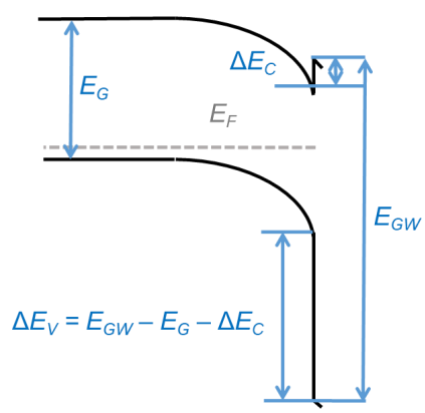

Figure 11. Band offsets that may affect solar cell performance. p-type absorber layer with band gap E_G is depicted with a CdS window layer of band gap E_{GW}.

Temperature-dependent V_{OC} is already in use to probe recombination characteristics [2] while avoiding the complexities of series resistance.[43, 44] In these methods, the V_{OC} versus temperature relationship, near room temperature, is extrapolated to its intercept

at absolute zero. The intercept voltage value (qE_a with q being the elementary charge) can be correlated with the location of recombination within the device, with a lower intercept indicating dominance by interfacial recombination and a higher intercept near the band gap ($qE_a \cong qE_G$) indicating dominance by bulk recombination. However, it has more recently been found that the value of qE_a can change with excitation, and this may be affected by the front junction band offset ΔE_C.[15]

For the molybdenum back contact used here, ohmic behavior is expected.[73] A barrier of 0.2 eV has sometimes been invoked to explain capacitance measurements in CIGSe,[74] although this is not necessarily large enough to significantly affect the JV characteristics. In particular, no rollover is visible in the forward J-V curve.

Sample Description: The 0.4275-cm^2 area solar cells were made of 2.5-μm thick $CuIn_{1-x}Ga_xSe_2$ absorbers deposited on a molybdenum-coated soda-lime glass substrate followed by a 70-nm window layer of CdS. The Mo back contact reflectance was taken as 0.3. For electrical measurements, devices were finished with a 210-nm ZnO/ZnO:Al bi-layer and Ni/Al grids.

The compositions are represented by x = Ga/(Ga+In). Two cells had an absorber composition of x = 0.50 and two cells had a composition of x = 0.35, without any gradient. Two additional absorbers were made with a standard Ga composition gradient, with a back-contact composition of x = 0.50, a front composition of x = 0.35, and a minimum of x = 0.25 at a depth of 0.5 microns from the front window layer. The respective band gaps for x = 0.50, 0.35, and 0.25 are E_G = 1.32, 1.24, and 1.17 eV.[75] Power conversion efficiencies greater than 15% were obtained in a solar simulator for the devices with graded absorbers.

Joint Electrical and Optical Analysis of CIGSe: A composition x = 0.50, non-graded sample will be labeled the baseline sample and its results used as a representative dataset. Its V_{OC}-T-I data are shown in Figure 12. To demonstrate the effect of each experimental variable on V_{OC}, the outcome of the numerical simulation is shown for several different values of that variable, while holding others fixed. In Figure 12 (a) we vary c_a. Increased absorber recombination reduces V_{OC}, whereas the intercept at the higher intensity, low-temperature limit remains approximately constant, in qualitative agreement with the intercept value (qE_a) method. In Figure 12 (b) the same experimental data are shown with the model outcome for increasing values of c_s. In this case, the intercept value falls, in qualitative agreement with the intercept value method.

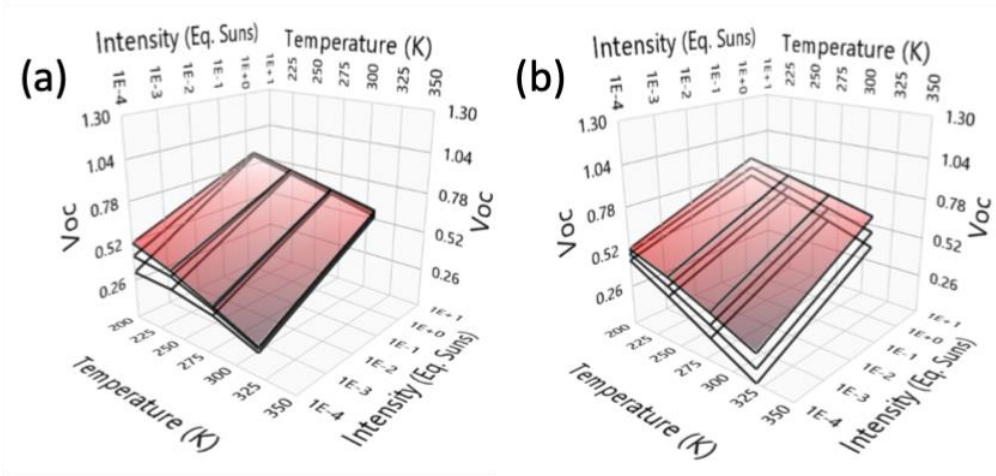

Figure 12. V_{OC} versus temperature and excitation intensity for the baseline sample. V_{OC} data is shown as a surface, and the grids are simulated V_{OC} values, with parameters varying as: (a) c_a is increased from 3.4×10^9 to 34×10^9 to 340×10^9 s^{-1}, and as (b) c_s is increased from 500 to 5000 to 50000 m/s. Each parameter increase, for both c_a and c_s, corresponds to a grid with a lower V_{OC}.

In Figure 12 (a) the same V_{OC}-T-I data are examined with the modeled outcome of changing ΔE_c from 0 to -0.1 to -0.2 eV, that is, from a continuous conduction band to a more cliff-like band offset at the window/absorber junction, as illustrated in Figure 11. The final, most cliff-like offset is the best match for the data. In Figure 12 (b) experimental data are shown from a separate, nominally identical device which was found to have a reduced V_{OC} at low intensity. This can be explained by shunt conductivity, since shunting is more important at low intensity.[53] The modeled outcome is shown with increasing shunt conduction, thereby producing a better match with the low-intensity data of the shunted device. The large difference in shunt conductivity is supported by the AC conductance from 1 kHz impedance measurement, which was 4×10^{-6} $\Omega^{-1}cm^{-2}$ for the non-shunted device and 100×10^{-6} $\Omega^{-1}cm^{-2}$ for the shunted device.

However, an Ohmic shunt could not account for the increase in V_{OC} at low temperature, nor could a space-charge limited current shunt (SCLC) mechanism.[39] Instead, a tunneling mechanism is more likely.

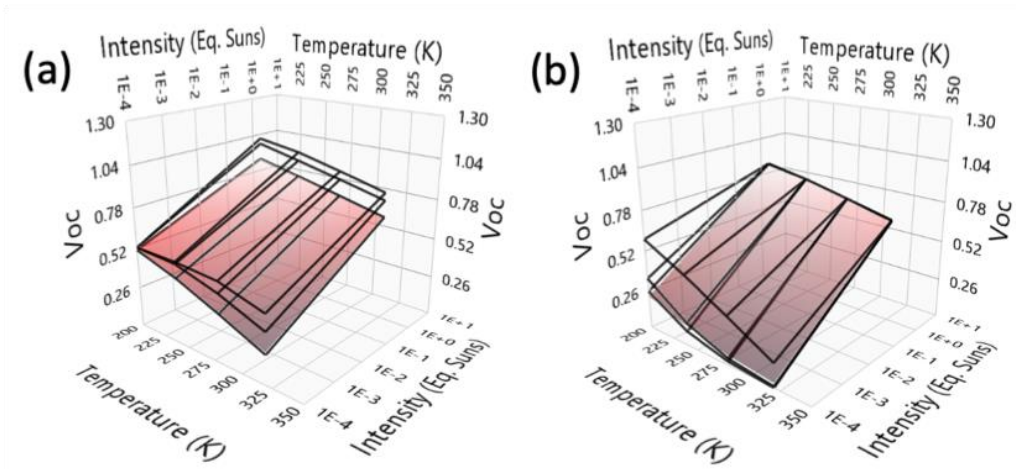

Figure 13. V_{OC} versus temperature and excitation intensity. V_{OC} data is drawn as a surface, and the grids are simulated V_{OC} values, with parameters varying as: (a) ΔE_C is changed from 0 to -0.1 to -0.2 eV, making it more cliff-like to match the data for the baseline sample, and (b) the shunting constant J_{T0} is increased from 4×10^9 to 40×10^9 to 400×10^9 cm^{-2} to match a nominally identical sample with increased shunt. Each parameter step, for both ΔE and J_{T0}, corresponds to a grid with a lower V_{OC}.

Tunneling current obeys a diode law in which the exponential function of the voltage does not depend on the ratio of voltage to temperature, so that $J_T = J_{T0}\exp(BT)\,(\exp(AV) - 1)$. The values of A = 6.5 $Volts^{-1}$ and B = 0.04 K^{-1} were taken from a reported analysis of the forward-bias kink in CIGSe dark JV curves.[76] Of course, obtaining a better fit to the JV curve alone would not convincingly demonstrate that tunneling current effects are present, as there are potentially other causes for a forward-bias kink, such as an inhomogeneous back contact barrier or a window layer with either spike-like offset or acceptor-like defects.[77-79] However, the low-intensity V_{OC} is difficult to explain without tunneling current, and the fact that the same parameters A and B can succinctly account for both JV kink and low-intensity V_{OC} phenomena is strong evidence that the tunneling current is a factor.

Varying two separate physical parameters can sometimes have overlapping effects on the V_{OC}, as seen in Figure 12 (b) and Figure 13 (a). To remove ambiguity, the PL intensity was also included in the least square fit. The PL intensity was converted to quasi-Fermi level splitting, and the data in Figure 14 and Figure 15 correspond to the same sample shown in Figure 12 and Figure 13. Data and modeled outputs are shown in Figure 13. also correspond to the same parameter variations shown in Figure 12 and Figure 13. Qualitatively, the PL-I measurements do not appear to be sensitive to c_s, Figure 14 (b), or shunting constant J_{T0}, Figure 15 (b). We see that c_a, Figure 14 (a), has a very different effect on the PL-I from that of ΔE_C. In general, V_{OC} is more sensitive to band offsets than PL-I is, whereas PL-I is more sensitive to overall recombination rate. The shunting constant has no effect on PL-I because PL-I is measured at a high injection level where the effect of shunt resistance is negligible.

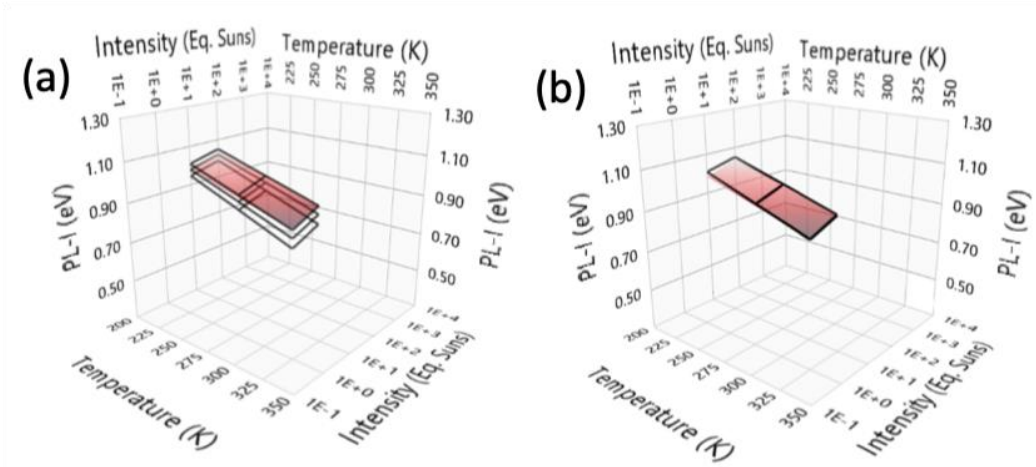

Figure 14. PL-I versus temperature and excitation intensity. Experimental PL-I data is drawn as a surface, and the grids are simulated PL-I values, with parameters varying as: (a) c_a is increased from 3.4×10^9 to 34×10^9 to 340×10^9 s^{-1}, and as (b) c_s is increased from 500 to 5000 to 50000 m/s. Each parameter increase, for both c_a and c_s, corresponds to a grid with a lower PL-I.

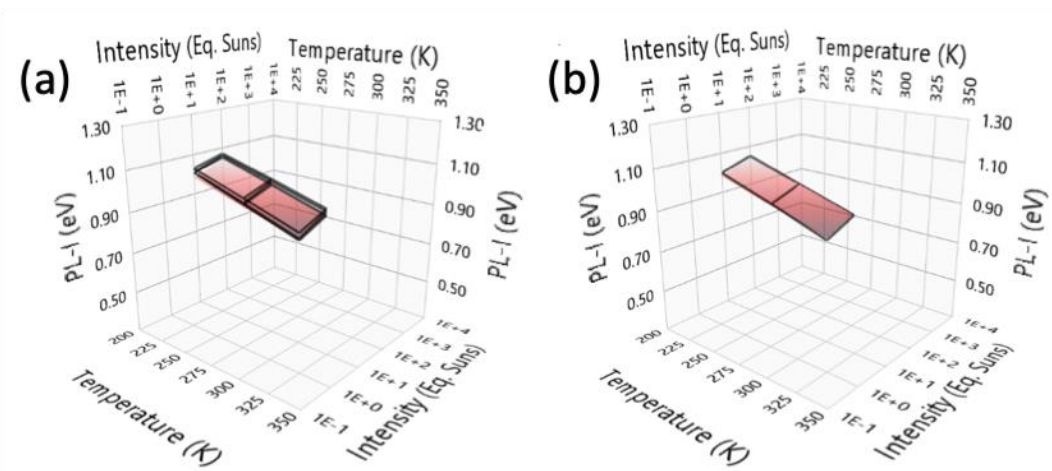

Figure 15. PL-I versus temperature and excitation intensity. Experimental PL-I data is drawn as a surface, and the grids are simulated PL-I values, with parameters varying as: (a) ΔE_C is changed from 0 to -0.1 to -0.2 eV, making it more cliff-like, and (b) the shunting constant J_{T0} is increased from 4×10^9 to 40×10^9 to 400×10^9 cm^{-2}. Each parameter increase, for both c_a and c_s, corresponds to a grid with a lower PL-I.

V_{OC}-T-I is highly sensitive to variations in shunt conduction which might not be evident through standard J-V curve measurement. To demonstrate this, pairs of nominally matching devices with differing shunt conduction values were identified for the x=0.50 composition, the x = 0.35 composition, and the graded composition. The resulting parameters for all three pairs are shown in Table 2. The second sample in Table 1 is the baseline sample. Those samples without a J_{T0} listed had negligible shunt conduction; fitting these instead to an ohmic model yielded >100 kΩ cm^2 shunt resistance, out of the range expected to appreciably affect a device's behavior. More importantly, the standard

lumped parameter shunting resistance would have appeared to be about 1 kΩ cm^2 for all samples, if the standard J-V slope analysis were used.[72, 80]

Table 2. Fitting results, showing negative (cliff-like) conduction band offset, absorber and interfacial recombination coefficients, and shunting constant.

x	ΔEc	c_a	c_s	J_{T0}
	eV	ns^{-1}	m/s	nA/cm^2
0.50	-0.19	3.44	500	0.4
0.50	-0.19	2.47	500	-
0.35	-0.18	1.21	100	1.2
0.35	-0.19	0.58	300	-
graded	-0.21	0.08	300	3.5
graded	-0.22	0.04	100	-

We find that c_a increases dramatically with composition. Within the graded absorber, the photo carrier concentration is expected to be the highest at the band gap minimum, which is the x = 0.25 minimum composition point. At the three compositions, x = 0.25, 0.35, and 0.50, the density of recombination center defects N_{ta} was indeed reported previously to scale upward with x, taking values of 1×10^{15}, 3×10^{15}, and 1×10^{16} cm^{-3}.[81] This suggests that the dominant recombination centers have a capture cross-section of about 10^{-14} cm^2. The band offsets are cliff-like, as expected when the x= 0.25 minimum is not in contact with the window layer. The fits are nonetheless dominated by absorber recombination, as reported for materials in this Ga composition range.[2, 82, 83]

Summary: The combined V_{OC}-T-I and PL-I analysis is found to be effective for determining key parameters needed for understanding band offsets, shunt resistance, and recombination in CIGSe solar cells. The V_{OC}-T-I method is very sensitive to shunt conductance, giving superior estimates when compared to a J-V curve analysis, which gives a lumped-parameter conductance that may conceal physical meaning. Absorber-window band offsets and recombination rates can also be extracted. Joint analysis of PL-I improves the determined parameter set, although it is necessary to quantify the PL signal in photon flux. PL-I is found to be less sensitive to shunt and band offset, but more sensitive to recombination, yielding a way to remove the ambiguity from band offset extraction. We consider this approach to be generally useful in complex device architectures where electrical and optical properties may both be studied.

Section 3: Report on studies emphasizing electrical or optical properties of solar cells. We carried out extensive studies of the electrical and optical properties of solar cells. These studies paved the way for the joint electrical and optical properties. Publication is noted.

Buffer/Absorber Interface Recombination Reduction and Improvement of Back-Contact Barrier Height in CdTe Solar Cells (Thin Solid Films doi.org/10.1016/j.tsf.2019.06.058)

In a generic CdTe device with architecture soda-lime-glass/transparent conducting oxide (TCO)/n_+-CdS buffer/CdTe absorber/back-contact, certain electronic and optical properties are key factors towards further improvement of device efficiency. Among these are the CdS/CdTe interface, defects, grain boundaries, and absorber/back-contact interface. In the CdS/CdTe solar cells, the portion of the solar spectrum with photon energies $\hbar\omega > 2.4$ eV, corresponding to the optical bandgap of CdS, is absorbed and does not contribute to the PV conversion. In addition, due to the band alignment between CdS buffer and CdTe absorber, significant interfacial recombination occurs at CdS/CdTe interface, which is due to the negative or "cliff-like" conduction band offset. To overcome absorption by the window layer, a higher bandgap material is desired to replace the CdS layer. ZnO is a good candidate window material since it has a high bandgap of > 3.1 eV and, consequently, will absorb less of the impinging solar radiation. Magnesium-doped ZnO (i.e., $Mg_xZn_{1-x}O$ or MZO) provides an additional degree of design freedom since the Mg composition (x) permits tuning of the bandgap. The lower electron affinity of MZO, relative to ZnO, is also desirable for the front-interface to form a "spike-like" conduction band offset between MZO and CdTe. This type of band offset is beneficial for reducing interface recombination. The cliff and spike band offsets are depicted in Figure 16. In addition to selecting the window layer, other factors for improving device performance include reduction of back-contact barrier height via CdTe back surface etching, post-annealing, and grain boundary passivation. The back contact in CdTe PV technology acts as a potential barrier to impede the hole transport. The impact of back-contact potential barrier is manifested in device parameters such as open circuit voltage (V_{OC}) and fill factor (*FF).* Post-deposition back-surface treatment and annealing play important roles in grain growth, recrystallization, stacking fault reduction, grain boundary, and defect passivation.

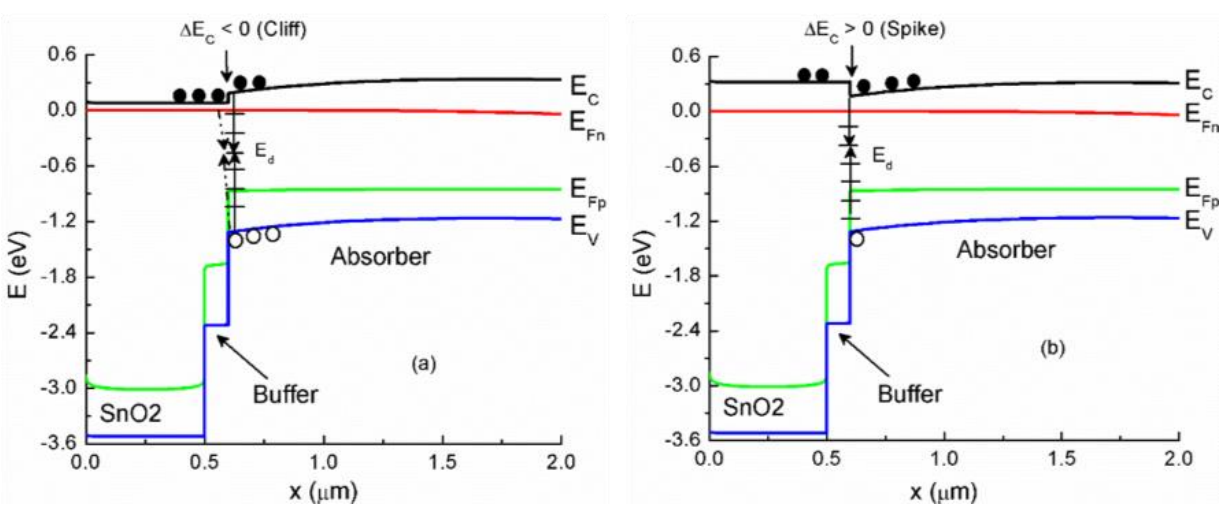

Figure 16. SCAPS-1D generated energy band diagram of CdTe solar cells that shows (a) cliff- ($\Delta E_c < 0$) and (b) spike-like ($\Delta E_c > 0$) positive conduction band offsets.

We have investigated electronic properties of a CdTe solar cell are reported using temperature-dependent capacitance spectroscopy and current-voltage characteristics, the latter in dark and illuminated conditions. The baseline solar cell material stack investigated is comprised of soda-lime-glass/SnO_2:F/SnO_2/CdS:O-buffer/CdTe-absorber/Cu/Au. Device properties are compared with CdTe solar cells in which the back surface was hydroiodic (HI) acid etched, before the back-contact formation, and a CdTe device in which Mg-doped ZnO (MZO) replaces buffer layers. Reduced back-contact barrier height and grain boundary barrier height are observed in the HI treated CdTe cell. Improved device performance in the MZO-based CdTe device is attributed to reduced emitter/absorber interface recombination when using the MZO window layer.

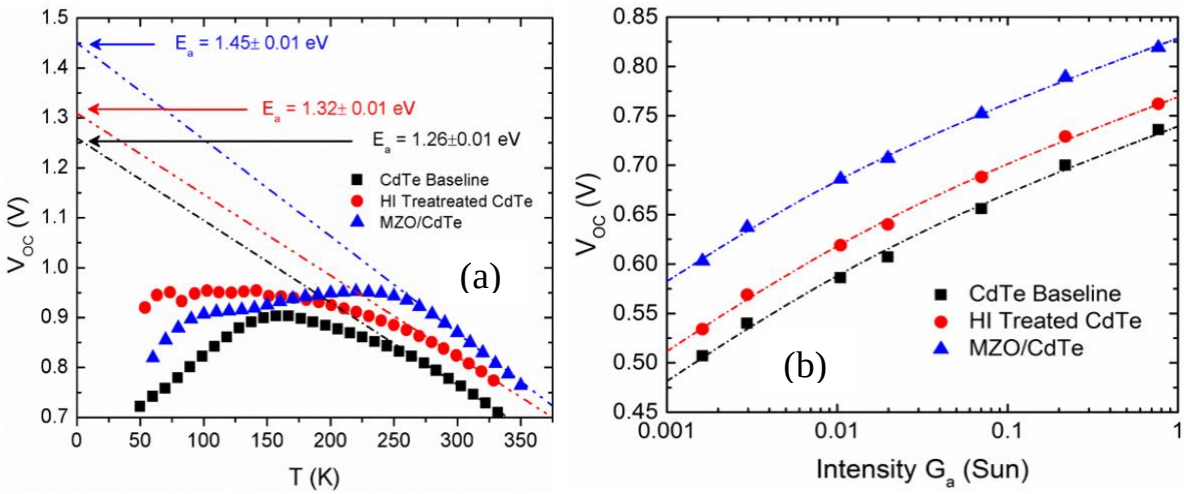

Figure 17. (a) Temperature dependence of V_{OC} for the CdTe cells studied shows the activation energy (E_a) of dominant recombination mechanism. We find E_a values of 1.26±0.01, 1.32±0.01, and 1.45±0.01 eV for baseline CdTe, HI treated CdTe, and MZO/CdTe cells respectively. (b) Intensity dependent V_{OC} on CdTe solar cells (CdTe baseline, HI treated CdTe, and MZO/CdTe) at T = 300 K to compare SRH recombination strengths: R^i, R^d, and R^b.

The comparable device parameters such as V_{OC}, J_{SC}, *FF*, and efficiency for all CdTe solar cells (CdTe baseline, HI treated CdTe, and MZO/CdTe) are summarized in Table 1. The HI treated solar cell device and MZO/CdTe device show an improvement in electrical parameters comparison to CdTe baseline.

Table 3. Photovoltaic and device properties of CdTe solar cells studied.

Device Properties	CdTe Baseline	HI Treated CdTe	MZO/CdTe
V_{OC} (V)	0.821	0.847	0.857

J_{SC} (mA/cm^2)	23.6	24.4	24.5
FF (%)	65.8	72.9	67.2
Efficiency (%)	12.9	15.1	14.1
E_a (eV)	1.26±0.01	1.32±0.01	1.45±0.01
Photon flux (photons/cm^2/s)	1.68×10^{17}	1.68×10^{17}	1.68×10^{17}
Absorber thickness (µm)	3.28	2.64	3.23
R^i(cm^{-2}s^{-1})	1.5×10^{13}	8.6×10^{12}	3.5×10^{12}
R^d(cm^{-2}s^{-1})	7.3×10^{12}	5.4×10^{12}	4.9×10^{12}
R^b(cm^{-2}s^{-1})	2.4×10^{13}	2.0×10^{13}	3.0×10^{13}
Lower temperature activation energy E_t from AS (meV)	83±3	39±2	96±1
Higher temperature activation energy E_t from AS (meV)	394±9	306±10	385±8
Activation energy $E_{a,\mu}$ of carrier freeze-out from mobility analysis (meV)	98±6	53±4	115±4
Back-contact barrier height Φ_{bc} from JV roll-over (meV)	402±6	309±7	381±7

While the temperature-dependent V_{OC} analysis alone provides only qualitative information on the dominant recombination in the absorber (at the front interface, in the depletion region, and in the bulk) the addition of intensity dependent V_{OC} analysis enables quantitative analysis. Using the combined temperature and illumination intensity dependent V_{OC} analysis, we can compare the strength of recombination (R_s) (mediated via defects, i.e., SRH type) at buffer/absorber interface (R^i), in the depletion region (R^d), and in the quasi-neutral region or absorber bulk (R^b) using the prior method. The estimated hole potential barrier heights are 0.94 eV, 0.89 eV, and 1.02 eV for CdTe baseline, HI treated CdTe, and MZO/CdTe solar cells respectively and these values are slightly lower than the standard First Solar CdTe cell (1.17 eV). At T = 300 K, illumination intensity dependence of V_{OC} for CdTe solar cells (CdTe baseline, HI treated CdTe, and MZO/CdTe) are presented in Figure *17* (b). Considering the photon flux of 1.68×10^{17} photons/cm^2/s (400 – 850 nm wavelength range), we find R^i, R^d, and R^b for the solar cells studied, as summarized in Table 3. In all cases, the R^b value is highest and relatively consistent across the three devices. The baseline device has a comparably high R^i which is consistent with the temperature-dependent V_{OC} analysis (i.e., from the activation energies of dominant recombination) where most of the generated carriers in the CdTe baseline device recombine at the buffer/absorber interface. A suppressed interfacial recombination in HI treated CdTe device is reflected in the reduced R^i value, which

suggests that hydroiodic acid may impact the buffer/absorber interface directly through grain boundaries or indirectly via assisting proper copper diffusion towards the buffer/absorber interface due to oxide removal at the back surface.

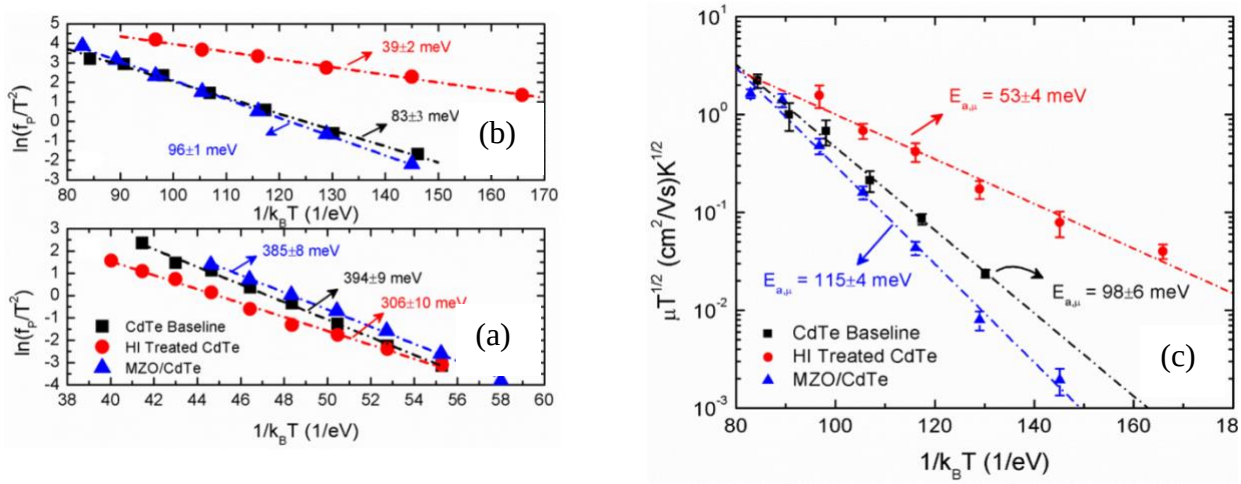

Figure 18. (a & b) Arrhenius plots from the admittance spectroscopic data are used to extract the activation energies in the carrier freeze-out effect and the back-contact barrier height of the investigated CdTe solar cells. (c) Temperature (80 – 140K) dependent hole mobility $\mu T^{1/2}$ vs $^{1}/_{k_B T}$ for CdTe baseline, HI treated CdTe, and MZO/CdTe solar cells to extract the mobility activation energies or grain boundary barrier heights.

We also utilize frequency- and temperature-dependent capacitance measurements (i.e., AS) to understand the energy of defects present. Figure 18 (a & b) summarizes the $ln\left({}^{f_P}/_{T^2}\right)\ vs.\ {}^{1}/_{k_B T}$ analysis for the CdTe baseline, HI treated CdTe, and MZO/CdTe devices. Activation energies of freeze-out conductivity [83±3 meV, 39±2 meV, 96±1 meV] and back-contact barrier heights [394±9 meV, 306±10 meV, 385±8 meV] correspond to the CdTe devices in the order of CdTe baseline, HI treated CdTe, and MZO/CdTe. To validate our estimation of the carrier freeze-out conductivity (i.e., the grain boundary barrier height), and the back-contact barrier height, we further explore AS-based charge transport (grain boundary barrier height) and roll-over feature in JVT characteristics (back-contact barrier height).

Extracted activation energies of mobility are 98±6 meV (baseline), 53±4 meV (HI treated), and 115±4 meV (MZO/CdTe). We also apply the (not shown) simple Arrhenius type mobility behavior, i.e., $\mu = \mu_0 exp\left(-\frac{E_{a,\mu}}{k_B T}\right)$ in which μ_0 is the temperature independent mobility pre-factor. Using this model equation, we find the activation energies of mobility for all solar cells: $E_{a,\mu}$= 93±4 meV (baseline), 49±4 meV (HI treated), 111±4 meV (MZO/CdTe). These estimated activation energies (or the grain-boundary barrier heights) are correlated, and in reasonable agreement, with the values observed in AS. The mobility activation energies in CdTe baseline and MZO/CdTe devices are in the same ~ 90-200 meV range reported in the literature. The activation energy observed in the HI

treated CdTe device is much lower, possibly due to passivation of grain boundaries which reduces the grain boundary potential.

Utilizing higher bandgap buffer materials, such as Mg doped ZnO, instead of conventional CdS buffer can potentially solve the problem of reduced recombination at the buffer/absprber interface. Using Mg-doped ZnO as the buffer layer enhances the solar absorption in the CdTe layer. While admittance spectroscopy is well known for defect study, it is also an electrical only method to study charge carrier transport study and extract grain boundary barrier height.

Electrical and optical characterization of CdTe solar cells with CdS and CdSe buffers—A comparative study (J. Vac. Sci. Technol. B https://doi.org/10.1116/1.5044219)

We study the combined electrical and optical properties of CdTe solar cells, prepared using CdS and CdSe buffer layers, to investigate defects in the bulk and interface, carrier transport, and recombination. Compared with the standard CdS/CdTe solar cell, it has been found that CdSe/CdTe cells show an enhanced photo-response in the short- and long-wavelength regimes and enhancement of the short-circuit current (J_{SC}). The higher solubility and stronger interdiffusion of Se through the CdTe absorber, when compared with S, leads to $CdTe_xSe_{1-x}$ alloy formation. The composition, structure, morphology, and photoactivity in the $CdTe_xSe_{1-x}$ alloy have also been investigated with various degrees of Se diffusion. Although higher photo-response and JSC were observed in the CdSe/CdTe device, it suffers notable open-circuit voltage (VOC) loss. This voltage limitation may be due to defects, bulk recombination, interface recombination, and nonohmic back-contact potential barrier. To identify and address these issues, combined electrical and optical characterization is necessary.

Temperature dependent capacitance–voltage (C–V) and admittance spectroscopy measurements extract carrier concentration, resistivity, charge carrier mobility, and their temperature dependence. Two defect signatures correspond to carrier freeze-out and the formation of a Schottky back-contact barrier. The back-contact barrier height (≈300 meV) extracted from the temperature dependent current density–voltage (JVT) experiment was confirmed by conventional admittance spectroscopy. Intensity dependent photoluminescence analysis demonstrates that the CdSe/CdTe device exhibits lower radiative efficiency than the CdS/CdTe device. This confirms the presence of higher defects in the CdSe/CdTe device corroborated by temperature dependent V_{OC} analysis. The comparative electrical and optical analysis provides insight into improving the performance of CdTe solar cell device by selenization.

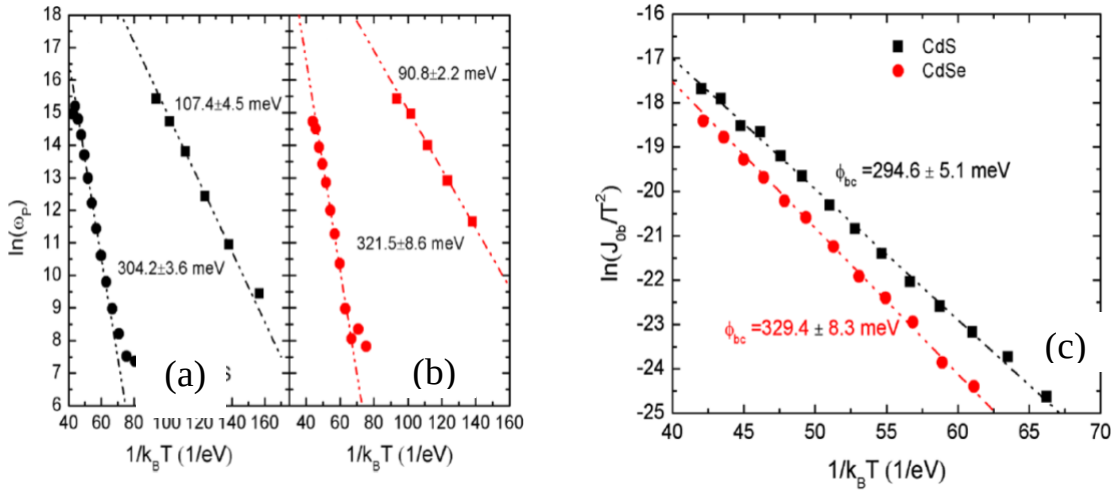

Figure 19. (a) & (b) $\ln(\omega_p)$ vs $1/k_BT$ plot to estimate the activation energy of defects at zero bias for CdS/CdTe and CdSe/CdTe devices. (c) Arrhenius plot [($J_{o,b}T^{-2}$ vs $1/k_BT$)] to extract the activation energy (φ_{bc}) which is the estimation of back-contact barrier height in CdTe solar cells using CdS and CdSe buffers.

Figure 19 (a &b) shows the activation energies determined from the Arrhenius analysis of the admittance peak frequency ω_P in the temperature dependent differential capacitance spectra (admittance spectroscopy). The ω_P values were extracted from two distinct minima corresponding to the signature of two defects (freeze out and Schottky back-contact barrier) in the temperature dependent differential capacitance spectra (not shown here). The low temperature ω_P represents the freeze out effect where high temperature ω_P represents back-barrier height effect. These are (107.4±4.5 meV and 304.2±3.6 meV) and (90.8±2.2 meV and 321.5±8.6 meV) for CdTe/CdS and CdTe/CdSe devices, respectively. The lower activation energies are attributed to the freeze-out of CdTe absorber conductivity. The higher activation energy is likely indicative of the potential barrier height of the back contact. We verify this in Figure 19 (c) by estimating the back-contact barrier heights in both cells using JVT measurements under dark conditions. The temperature dependent $J_{0,b}$ values are extracted from rollover feature in the JVT curve using Richardson-Schottky formula.

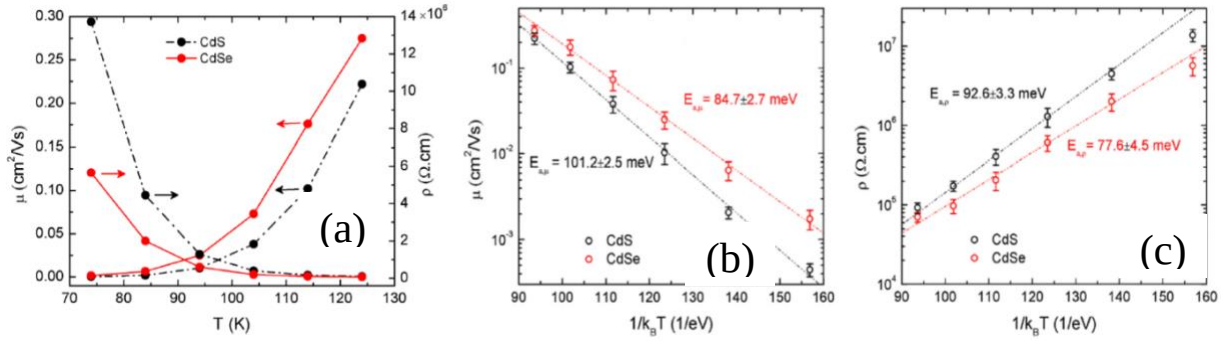

Figure 20. (a) Temperature dependent mobility and resistivity in CdTe solar cells with two different buffer layers (CdS and CdSe). Arrhenius plots of temperature dependent hole mobility (b) and resistivity (c) to estimate the mobility and resistivity.

Figure 20 (a) shows the temperature dependence of hole mobility and resistivity in the CdTe devices in the range 74-124 K. With increasing temperature, the measured mobilities increase with the expected concomitant decreases in resistivity. The observed temperature dependent mobility and resistivity trends agree with literature reports for a polycrystalline CdTe material. In the temperature range of Figure 20 (a), the mobility and resistivity follow the Arrhenius dependence, $\mu \sim exp\ (-E_{a,\mu}/k_BT)$ and $\rho \sim exp\ (E_{a,\rho}/k_BT)$, where $E_{a,\mu}$ and $E_{a,\rho}$ are the activation energies of the mobility and resistivity, respectively, as shown in Figure 20 (b & c). The extracted activation energies of mobility are 101.2±2.5 meV and 84.7±2.7 meV for CdS/CdTe and CdSe/CdTe devices, respectively. Similarly, the extracted activation energies of resistivity for CdS/CdTe and CdSe/CdTe devices are 92.6±3.3 meV and 77.6±4.5 meV, respectively.

The polycrystalline semiconducting materials consist of variable sized grains and defective grain boundaries which has a significant impact on the energy band and consequently for *p*-type semiconductors downward band bending occurs and leads to a potential barrier. This potential barrier hinders the motion of holes in the valence band so that activation energies of mobility and resistivity in our CdTe absorber can be representative of grain boundary barrier height in samples due to its polycrystallinity. Previous studies reported the presence of charged grain boundaries in CdS/CdTe solar cell devices and estimated a grain boundary height in the range 90–200 meV. Accordingly, using $\ln(\mu T^{\frac{1}{2}})$ vs $1/k_BT$ plots, then we get mobility activation energies 104.5±2.5 meV and 86.9±2.4 meV for CdS/CdTe and CdSe/CdTe, respectively. Similarly, using the $\ln(\rho T^{\frac{1}{2}})$ vs $1/k_BT$ analysis, we estimate that the activation energies of resistivity for CdS/CdTe and CdSe/CdTe devices are 94.1±1.9 meV and 81.9±4.4 meV, respectively. Our extracted activation energies are consistent with reported grain boundary height range and indicated that the potential barrier height can be a strong factor for the observed temperature dependence of mobility and resistivity in the temperature range 74–124 K. We also note that activation energies of mobility and resistivity for the CdSe/CdTe device are lower (~16 meV) than the CdS/CdTe device. This can be attributed to the difference in the grain boundary barrier height as a function of grain size.

We also performed photoluminescence intensity (PL-I) measurements on samples to compare the optical performance of CdS/CdTe and CdSe/CdTe devices. The excitation power density range was varied from 10^{-1} W/cm^2-10^{+3} W/cm^2 using 2.41 eV and 1.88 eV excitation photon energies. The PL intensity of CdSe/CdTe device is remained lower than CdS/CdTe device in the studied excitation power density range, suggests that non-radiative recombination rate is higher in CdSe/CdTe due to higher defect density.

The combined electrical and optical characterization provide insight into the properties of CdSe-buffered and CdS-buffered solar cells. The investigations address active defects, transport properties, and recombination in the bulk and interface regions. Carrier density profiles in CdS/CdTe device, obtained via CV and DLCP, are found to agree each other. However, there is dissimilarity in the CdSe/CdTe device, which is attributed to the presence of defects in the bulk of CdTe absorber. Differential capacitance versus temperature spectra show two defect signatures for each sample at low and high temperature. For both devices, defects associated with the low- and high- activation energy are related to freeze-out of the CdTe absorber and presence of a non-ohmic back-contact, respectively. Defect energies extracted from the admittance spectroscopy and JVT measurements are in good agreement. The temperature dependence of mobility and resistivity in both cells shows activation energies of mobility and resistivity are related to the band fluctuation or grain boundary barrier height. PL-I measurements, which are sensitive to non-radiative recombination, show much lower radiative efficiency in CdSe/CdTe cell which is attributed to higher energy defects.

Electrical properties of CdS/Cu(In,Ga)Se2 interface (Jpn. J. Appl. Phys. doi.org/10.7567/JJAP.57.085701)

Interfaces are crucial to all photovoltaic (PV) devices because they typically consist of multiple layers of heterogeneous materials and strongly affect recombination. The most important interfaces in thin-film PV devices are those next to the main junction of the absorber where the quasi-Fermi level separation sensitively determines the open-circuit voltage V_{OC}. Most well-known is the prototypical CdS/absorber interface where the choices of absorber include Cu(In,Ga)Se$_2$ (CIGS), CdTe, and Cu$_2$(Zn,Sn)Se$_4$—the former two being the most advanced and commercialized thin-film PV technologies. We have studied the CdS/CIGS interface keeping in mind that the methodology and results may be transferable to other interfaces with the absorber. Optimization of interfaces requires a thorough understanding of their electrical properties: the energetic distribution of interface states in the bandgap, i.e., density of states D_{it} their capture cross-section σ; fixed charge at the interface Q_f; and surface recombination velocity.

We demonstrated the extraction of D_{it} and Q_{it} at the CdS/CIGS interface from a mercury-probed high-frequency CV technique applied to an MIS structure. We use the AS technique to measure E_F at the interface (i.e., the inversion strength) and $\gamma \equiv \sigma \cdot v_{th}$ of the interface states. We use a simplified Shockley–Read–Hall recombination formulation to calculate the surface recombination velocity from parameters directly measured by CV and AS. The calculated surface recombination velocity value compares well with that extracted from the recombination analysis by the $V_{OC}(T,I)$ method. The methods and results presented in this work provide in-depth understanding of the CIGS interfaces and enable future passivation studies.

Absolute photoluminescence intensity in thin film solar cells (J. Appl. Phys. doi.org/10.1063/1.5064798)

Luminescence imaging is a measurement technique used for development and rapid assessment of photovoltaic devices. Since the luminescence intensity has an exponential dependence on the quasi-Fermi level splitting between electrons band holes, the implied open circuit voltage can be probed even before the fabrication of an electrical contact structure. A critical aspect of this is the need for quantitative measurement of the PL intensity at the sample. Although there are reports in the literature stating this was done, they lack the detail needed to reproduce the measurements.

Previous work has related ΔE_F to absolute measurements of PL magnitude (in photons/m^2/s) by way of the "Lasher-Stern-Wurfel" (LSW) formula. By carrying out spectrally resolved PL and restricting the analysis to higher energies where $\alpha(E)$ is large, the energy-dependent PL gives ΔE_F without reference to thickness or $\alpha(E)$. However, ambiguities and unrealistic results often follow from the precise choice of high energy range for $\alpha(E)$. Authors have attempted to instead fit the entire PL spectrum, although this relies on adopting an uncertain absorption tail model at low energies. One alternative is to use the full, integrated PL intensity. This would no longer allow the assumption of $a(E) = 1$, but small non-uniformities would not be amplified by extrapolation, and the overall intensity should be fairly insensitive to the precise details of low energy tailing.

Since the total luminescence efficiency of a solar cell is directly related to its power generation efficiency, a number of calculations have already been put forward for the absolute emission rate of photons from a layered structure. Re-absorption and multiple front and back interface reflections should be considered as well as the angular and spectral dependence of the reflection and absorption. While interference is typically ignored with the use of ray optics, it can become significant with thin films, particularly those with a composition grading that changes over length scales on the order of wavelength. Surprisingly, there does not appear to be any reported calculation relating radiative recombination rates within layered structures to external emission rates, in a quantitative way which accounts for interference and re-absorption.

We have calculated the external emission of luminescence from an excited semiconductor within a layered structure of known optical properties. The absolute emission caused by a given value of ΔE_F at a given location is taken from the LSW formula, and Sipe's Green's functions are used to find the impact of the structure on the external emission from a randomly oriented dipole radiation source at that location.

For validating this model, we need to relate the number of photons to a raw detector signal, a standard source of known absolute radiant flux is needed. Although there are reports in the literature stating that this type of intensity calibration has been performed, they are not sufficiently detailed to permit straightforward reproducing of the method. We devised and reported our own approach in which the excitation laser is focused onto a Spectralon reflectance standard, which has a reflectance of nearly unity with a highly diffuse character. When illuminated with a laser spot of intensity I, the surface of the reflectance standard forms a Lambertian source with radiance I/π. The rate of photons passing through the aperture in this case would be

$$R_{ref} = \mathcal{A}\int_0^{2\pi}\int_0^{\theta_{obj}} \cos\theta \frac{I}{\pi\hbar\omega_L}\sin\theta\,\mathrm{d}\theta\mathrm{d}\varphi = \frac{\mathcal{A}I}{\hbar\omega_L}\sin^2\theta_{obj}$$

where $\hbar\omega_L$ is the photon energy of the laser light. The power $\mathcal{A}I$ can be measured with a power meter, yielding a known R_{ref} for that aperture and laser intensity. A conversion factor C is then found by setting the detector signal (in V_{out} or current) equal to CR_{ref}, to account for detector responsivity and any optical losses between the sample surface and the detector. C is also multiplied by the ratio of the detector responsivity at the PL wavelength to the detector responsivity at wavelength 660 nm for the laser. When measuring PL, this allows us to equate the detector signal to CR, obtaining ΔE_F. The simplified experimental setup is depicted in Figure 21.

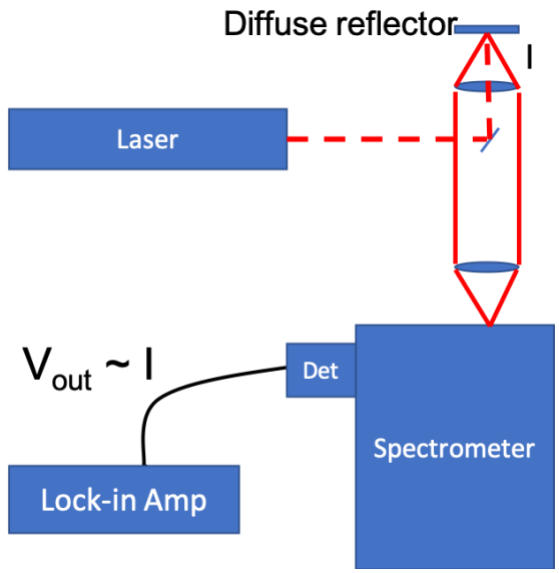

Figure 21. Essential elements of quantitative PL intensity measurements for PL-I or spectroscopy. The laser is reflected by a known diffuse reflector (Spectralon) so that amount of light incident (laser, measured) and that collected by the optics (I) are determined by solid angle.

The approach was validated using CIGS solar cells prepared at NREL. An important practical limitation was discovered. The PL intensity is only measurable when using sufficiently high laser power (density). The standard VOC approach for measuring quasi-Fermi-level splitting was only possible at lower intensity. Therefore, we “stitch” the two measurement regimes together in Figure 22. Despite the limitation, we validate from this work that the PL-I approach satisfactorily agrees with the electrical measurement across the differing intensity regimes. Future application should address materials that give hearty PL intensity at lower excitation.

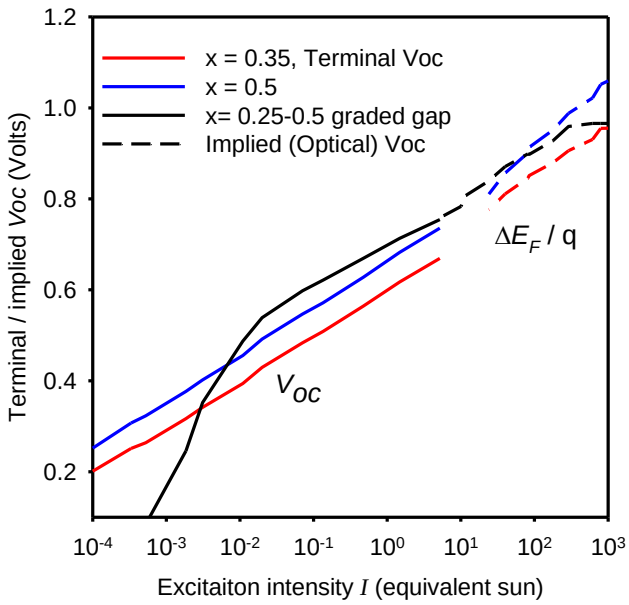

Figure 22. Comparison of the measured open circuit voltage to the quasi-Fermi level splitting extracted directly from measured PL intensity without free parameters. An intensity of 1.7×10^{17} photons cm^{-2} s^{-1} is labelled as an equivalent sun.

Investigation of cadmium telluride grown by molecular beam epitaxy using micro-Raman spectroscopy below and above the laser damage threshold (J. Vac. Sci. Technol. B doi.org/10.1116/1.5048526)

This work was motivated by indirect evidence that PL measurements could be degrading samples due to laser intensity. Similarly, Raman spectroscopy shows laser-induced degradation of CdTe during the measurement. This undesirable effect limits the usefulness of PL and Raman studies, as well as other optical techniques commonly using laser excitation.

The advent of highly sensitive Raman systems makes the approach prospectively useful, provided it is demonstrated that laser damage is not taking place. In this report, the effects of visible laser light on cadmium telluride (CdTe), grown by molecular beam epitaxy, are studied at low (48 μW/μm^2) and high (480 μW/μm^2) laser power densities using micro-Raman spectroscopy. The Raman spectrum of CdTe shows no notable change at low power density ~48 μW/μm^2 for prolonged laser exposure. At higher power density ~480 μW/μm^2, the Raman spectrum is significantly changed, and strong Te-related peaks appear in the spectrum, even for short laser exposure times suggesting that photo induced Te enrichment happens at the CdTe surface at high laser power density. The temperature rise is estimated from observed shifts in the Te and CdTe optical phonon peaks and modeled using finite-element simulations. At laser power 480 μW/μm^2, the CdTe exhibits a rise of ~44 °C above room temperature while the observed change in Te temperature is significantly higher, ~179 °C. Ours is the first report of systematic temperature rises and their differences in the Te and CdTe.

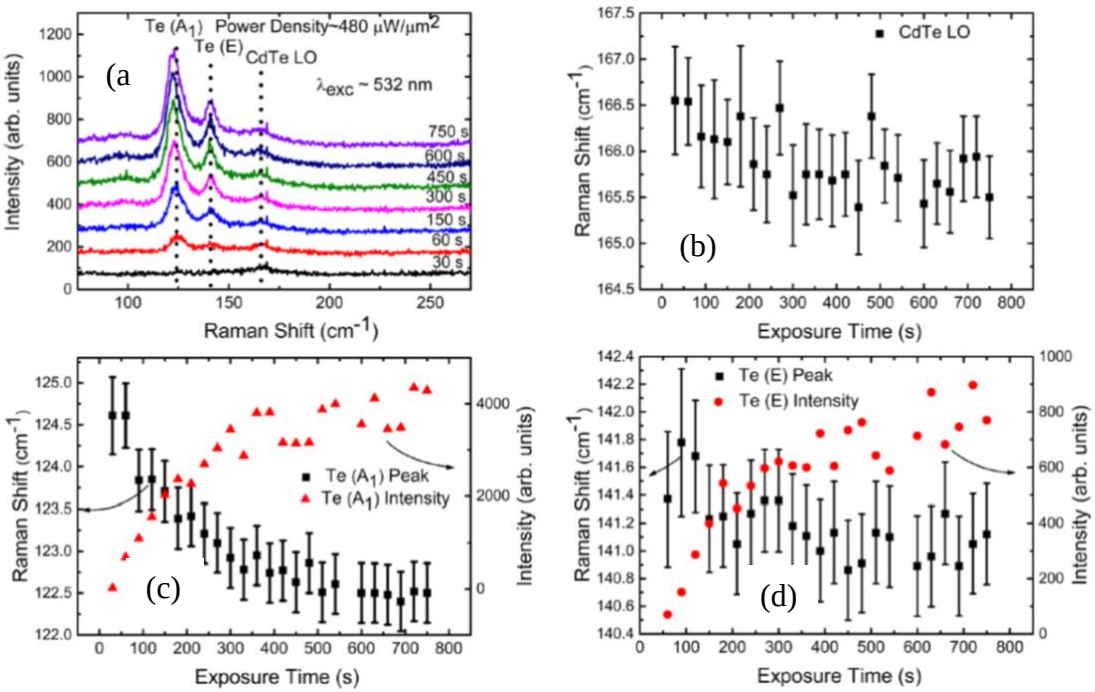

Figure 23. (a) Micro-Raman spectra for different laser exposure times at power density 480 μW/μm^2. The dashed lines highlight the peak position of Te(A_1), Te(E), and CdTe LO phonons. (b) Raman shift of CdTe (LO) phonons vs exposure time. (c) Raman shift of Te (A_1) phonon (left-axis) (symbol: black square) and intensity (right-axis) (symbol: red triangle) vs exposure time. (d) Raman shift of Te(E) phonon (left-axis) (symbol: black square) and intensity (right-axis) (symbol: red circle) vs exposure time.

Figure 23 presents the Raman results taken at power density ~ 480 μW/μm^2, also for different exposure times. We prescribe an approach for establishing the onset of laser damage. A total of 25 sequential Raman spectra were recorded, each with 30 s acquisition time, for a grand total laser exposure time of ~ 750 s. We present representative Raman spectra in Figure 23 (a). For the early exposure times (~ 30 s), we observe the CdTe LO phonon at 166.55±0.47 cm^{-1} and very weak peak near 124.5 cm^{-1} close to the baseline intensity. As the exposure duration continues to grow, intensity of the peak around 124.5±0.5 cm^{-1} clearly increases and a new peak ~ 141.4±0.5 cm^{-1} appears in the spectra, illustrates the laser damage effect on surface of CdTe. These two peaks have been previously reported and are assigned to A_1- and E-symmetry, zone-center phonons of crystalline Te. From fits to the spectra we observe a change in the peak position of CdTe LO-phonon position. Although the variations are very small, the gradual trend observed in Figure 23 (b) shows a red shift with exposure duration. As discussed below, the observed red shift can be attributed to laser heating of the CdTe. The Te peaks are similarly examined. We summarize the A_1 and E peak positions and intensities, versus exposure time, in Figure 23 (c) and (d). The systematic red shifts similarly indicate gradual sample heating. The line widths of the phonon peaks studied do not show any trend with exposure time. When the power density is reduced ~ 48 μW/μm^2 at different spot on surface, we do not observe the Te related peaks in the Raman spectra of CdTe for long exposure time up to 90 mins. Also, the CdTe LO

phonon peaks do not shift with exposure time, suggests that power density ~ 48 μW/μm^2 is below the laser damage threshold.

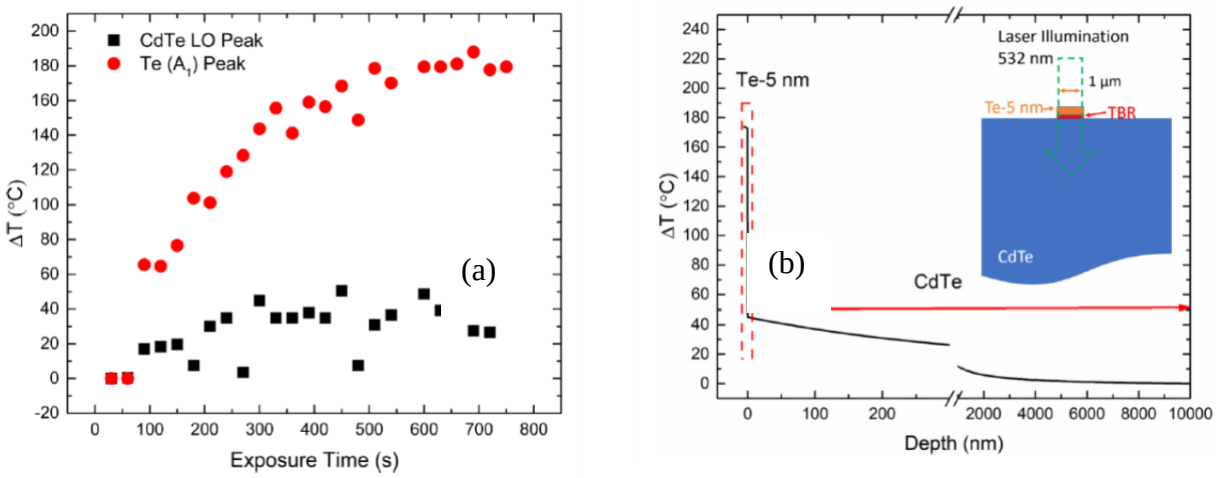

Figure 24. (a) Temperature rise vs exposure time for CdTe LO (symbol: black square) and Te phonons (symbol: red circle). (b) Simulated temperature rises relative to room temperature vs depth. Dashed rectangle denotes near-surface region of interest. Inset depicts the simulated geometry. The TBR stands for thermal boundary resistance.

Figure 24 (a) represents the temperature rise in Te and CdTe. The temperature rise is estimated from shift phonon peak position in Figure 23 and the phonon coefficient of Te from Ref.[10] and CdTe respectively. The Te temperature rise is significantly greater than what is observed for the CdTe during high power laser exposure time in Figure 24 (a). This is explained based on the high absorption coefficient of Te (~ 5×10^5 cm^{-1}), compared to CdTe (~ 8×10^4 cm^{-1}) at 532 nm excitation wavelength, resulting in more laser power absorbed by the Te when it is present at the surface as a thin film or as islands at the surface or within the near-surface region. One consequence of this scenario is that the initial composition of a CdTe sample plays an important role in any laser-induced Te formation, which may explain diversity in reports of laser heating. Further, if the Te enriches due to laser exposure, the high optical absorption will increase the local heating of the Te relative to the CdTe. Our estimated temperature rise ~179 °C, based on Te phonon shift at higher laser power density, which is below the melting point of Te, suggests that Te thermal migration is not a possible cause for Te enrichment on surface. Another factor that may effectively enrich Te is Cd sublimation under laser illumination, a process which may occur around 200 °C.[13]

To examine laser heating at higher power density as a cause of the observed temperature rises, we also performed finite-element simulations using COMSOL multi-physics. The simulated temperature rises in Te and CdTe were found to be sensitive to these thermal boundary resistance of layers (CdTe/Te) and thermal conductivity of CdTe. This simulation shows that asymmetric heating of the surface Te and CdTe is readily achieved, as seen in the simulated temperature profile of Figure 24. To estimate the observed temperature rise in CdTe, we compute a weighted average of the depth-dependent temperature rise (ΔT) above ambient within the CdTe according to $\langle \Delta T \rangle = \frac{\int \Delta T(x) \exp(-\alpha x) dx}{\int \exp(-\alpha x) dx}$

where $\Delta T(x)$ is the simulated temperature rise as a function of depth x in the CdTe and α is its optical absorption coefficient at wavelength 532 nm. The estimated $\langle \Delta T \rangle$ = 44 °C of CdTe is obtained when using thermal conductivity of 4 W/m/K for CdTe; the temperature rise of 174 °C within the simulated Te layer was obtained with a TBR ~ 3.5×10^{-7} m^2 K/W. The thermal conductivity of CdTe is lower than the accepted value ~7 W/m/K.[14,15] Ref.[14] suggests that lower crystalline quality and defects may reduce thermal conductivity in their comparative study of thermal properties of poly and single crystalline CdTe materials. In our study, we note that unpassivated CdTe, grown by MBE, is highly susceptible to near surface defects. Furthermore, the value we obtain is for CdTe which has been denatured by the local laser heating. Both of these factors are expected to reduce the thermal conductivity of the CdTe. We find no reports of the TBR between CdTe and Te. The value obtained here is high in comparison to what has been generally reported for materials.[16] This suggests the Te is in poor thermal contact the CdTe.

This report provides a needed approach for evaluating the damage threshold to CdTe.

Conclusions

Joint electrical and optical analysis has been developed. Electrical measurements focused on V_{OC}(T,I). Optical analysis focused on PL-I(T,I), which was a revision of the initially planned PL spectroscopy. The PL(λ,T,I) analysis required absolute intensity measurements. A custom simulation program was prepared to consistently fit the V_{OC}(T,I) and PL-I(T,I) manifolds based on fundamental semiconductor physics and with fitting parameters related to recombination rates. Outcomes were cross-checked using extensive electrical characterization including admittance spectroscopy. Results have been published. We conclude with review of the milestones.

Year 1 Milestones

1. Established readiness for instrumentation and methodology development: i) V_{OC}(T,I) and PL(λ,T,I) setups operational with 1000:1 intensity adjustability and demonstrated by collecting V_{OC} (T,I) and PL(λ,T,I) raw data from at least one existing CdTe solar cell; ii) extraction of modeling input parameters $E_g(x)$ using spectroscopic ellipsometry to within 5% agreement with Auger electron spectroscopy and $E_F(x)$ with 1 meV resolution; and iii) 4 CIGS (from NREL or a similar source) & 4 CdTe (from University of Toledo or a similar source) solar cells fabricated, together with 4 CdTe solar cells from First Solar and 8 Si solar cells from NREL or similar and one other institution (e.g. Arizona State University or similar), with best interfaces arrive at Texas State University.

These milestones were completed during the grant period with the exception of involvement by institutions not funded by the award.

2. For the ideal scenario, the depth profiles of radiative and Shockley-Read-Hall recombination $R_{rad}(x)$ and $R_{SRH}(x)$ are solved, using measurement factor MF(x) calibrated in devices with uniform bandgap to achieve within 5% agreement between optically- and electrically-extracted Fermi energy splitting. Buffer/absorber films (6 CIGS from NREL or similar and 6 CdTe from University of Toledo or similar) and devices (6 CIGS from NREL or similar and 6 CdTe from University of Toledo or similar) arrive at Texas State University for next-stage development.

These milestones were completed during the grant period.

3. For the approximate scenario, the depth profile of radiative recombination $R_{rad}(x)$ is solved using segmental approximated quasi-Fermi level profiles that agree with $S_{i,f}$ by capacitance-voltage measurement on metal-insulator-semicondcutor structure to within a factor of 3. CIGS and CdTe baselines devices (6 CIGS from NREL or similar and 6 CdTe from University of Toledo or similar) arrive at Texas State University.

These milestones were completed during the grant period.

4. For the approximate scenario, the depth profile of Shockley-Read-Hall recombination $R_{SRH}(x)$ is solved with a spatial resolution $\delta x<50$ nm and dynamic range $R_{SRH,max}/R_{SRH,min}>10$ and calibrated with J_0 method to within a factor of 3 in Si devices. Buffer/absorber films (6 CIGS from NREL or similar and 6 CdTe from University of Toledo or similar) arrive at Texas State University for next-stage development.

The spatial-resolution milestones were completed during the grant period with the understanding that the depth resolution is at the interfaces within the device material stack and not at an arbitrary position within, say, the buffer layer. The dynamic range milestones were not met.

Go/No-Go

Development of the metrology for obtaining the depth profiles of the radiative and Shockley-Read-Hall recombination $R_{rad}(x)$ and $R_{SRH}(x)$ with a spatial resolution $\delta x<50$ nm and dynamic range $R_{SRH,max}/R_{SRH,min}>10$ for the approximate scenario in thin-film PV devices. Results calibrated with J_0 method to within a factor of 3 in Si devices to achieve 25 mV sensitivity in V_{OC} change.

The Go/No-Go was passed.

Year 2 Milestones

1. For the exact-solution scenario, the depth profile of radiative recombination $R_{rad}(x)$ is solved using the exact solution of quasi-Fermi level profiles $E_{FP}(x)$ and $E_{FN}(x)$ that agree with $S_{i,f}$ measured by capacitance-voltage measurement to within a factor of 3.

These milestones were completed during the grant period.

2. For the exact-solution scenario, the depth profile of radiative recombination $R_{rad}(x)$, $S_{i,f}$, and $S_{i,b}$ are solved with a spatial resolution $\delta x<20$ nm, dynamic range $R_{j,max}/R_{i,min}>100$ and calibrated with J_0 method to within 50% in Si devices. At least 1 version (6 samples each from NREL or similar and Toledo or similar) of improved baseline CIGS or CdTe devices arrive at Texas State University.

These depth-resolution milestone was completed as it relates to interfaces. Additional devices were delivered.

3. Region of most interest identified. At least 1 version of CIGS baseline devices (6 samples from NREL or similar) improved in V_{OC} by 25 mV per guidance by the metrology. Maximum available V_{OC} improvements in CdTe cells have been predicted by the metrology.

The regions of interest were identified as absorber layer and back contact. Properties were extensively studied. Predictions were not completed.

4. Region of most interest (i.e. with the highest recombination rates) identified in currently available CIGS and CdTe cells. At least 1 version of CdTe baseline devices (6 samples from Toledo or similar) improved in V_{OC} by 50 mV per guidance by the metrology. Maximum available V_{OC} improvements in CdTe cells have been predicted by the metrology.

The regions of interest were identified as absorber layer and back contact. Properties were extensively studied. Predictions were not completed.

Year 3 Milestone (revised)

1. Conduct measurements and write manuscripts according to revised SOW.

This milestone was completed primarily during the grant period but with additional manuscript authorship taking place after the award period.

Budget and Schedule

Information on the project budget is included in the table. Deviation in the spend plan occurred at the beginning of budget period 3 due to a reduction in support.

Budget Categories per SF-424a	**Actual Cumulative**
a. Personnel	$276,255
b. Fringe Benefits	$96,750
c. Travel	$9,372
d. Equipment	$72,160
e. Supplies	$53,085
f. Contractual	$255,538
g. Construction	$0
h. Other	$4,332
i. Total Direct Charges	**$767,492**
j. Indirect Charges	$185,266
k. Total Charges	**$952,758**
Cost Share	$173,100
Cost Share Percentage	18.2%

Path Forward

The CIGS community in Japan exhibited a genuine interest towards the methodology of our research project. In particular, the research groups of T. Sakurai and Minemoto, respectively. The researchers have separately engaged in conversation/visit with Dr. Li on this subject after Li's move to Taiwan. It is apparent that they are independently experimenting with similar techniques.[84, 85] Specifically, the wavelength-dependent J-V analysis (with intensity dependence) appears to have a close resemblance to work

conducted in this project. This helps validate and value of the technique developed in this project.

Regarding the barriers to its wider application in the PV community, the PLI experiment setup is not common, although it is not particularly costly. An issue experienced during our work was low intensity of PL from the solar cell materials, particularly any commercial structures. This prohibited PL spectroscopy as originally planned, and permits PL-I over only a relatively high excitation intensity regime that is beyond the range where electrical measurements are conducted. It may be worthwhile to investigate “hero” CdTe cells that exhibit “strong” PL to see if these issues—PL spectroscopy not being possible and PL-I only agross a narrow range—can be mitigated. Greater overlap between the intensity rebime where V_{OC} and PL-I can be carried out will also help better in validating simulations. The simulations are a necessary cornerstone of this techniqjue. Further work is needed in the numerical computation/simulation methods to reduce the initial threshold of adoption.

A new challenge that arose at the end of the project was unintentional band gap grading caused by diffusion. In our case, a CdSe interlayer of unknown thickness was used at the window contact on a CdTe absorber, and the CdSe spread throughout the absorber during later processing steps. The distribution of the spread was unknown. Unlike the graded gap of CIGS absorbers, Auger or SIMS measurements of the composition were inconclusive. PL measurements were able to give us the average Se content in the ~ 120 nm close to the CdTe/CdSe interface. External quantum efficiency measurements are useful to find the band gap minimum which dominates the recombination, and these were in agreement with the PL. Since the necessary optical properties of the CdSeTe alloy system are now established, it may be still be possible to gain accurate results about band offsets through simplifying assumptions about the absorber and its gap minimum.

The Texas State University principal investigator is dedicating near-future research plans to thermal properties of materials and the integration of diamond with semiconductor materials and devices for thermal management. Two undergraduate, two M.S., and one Ph.D. students, along with three postdoctoral associates, were each partially supported. Each of these is continuing their career in applied materials physics.

The principal investigator at National Cheng Kung University is dedicating near-future research efforts to Ga_2O_3.

NREL plans to pursue higher V_{OC} in CIGS solar cells through alkali treatments and adjusting the bandgap grading. The research from this project has helped inform PL measurements that are ongoing at NREL so that quantitative voltage loss analysis is available for use in thin-film projects.

University of Toledo: CdTe solar cells using ZnMgO buffer layer showed improved V_{OC}. University of Toledo plans to optimize the composition, post-deposition treatment, and thickness to further improve the Voc.

Publications Resulting from This Work

Full citation information is in the reference section below for those publications in print.

2017		
[15] Brandt et al.	Determining interface properties limiting open-circuit voltage in heterojunction solar cells	J. Appl. Phys
[16] Sohal et al.	Carrier Lifetimes of Iodine-Doped CdMgTe/CdSeTe Double Heterostructures Grown by Molecular Beam Epitaxy	J. Electronic Mater.
2018		
[17] Li et al.	Electrical properties of CdS/Cu(In,Ga)Se_2 interface	Jpn. J. Appl. Phys.
[18] Sohal et al.	Investigation of cadmium telluride grown by molecular-beam epitaxy using micro-Raman spectroscopy below and above the laser damage threshold	J. Vac. Sci. Technol. B
[19] Mia et al.	Electrical and optical characterization of CdTe solar cells with CdS and CdSe buffers—A comparative study	J. Vac. Sci. Technol. B
[20] Paul et al.	Study of charge transport properties in a ZnO/CdS/Cu(In,Ga)Se_2 solar cell via admittance spectroscopy	J. Vac. Sci. Technol. B
2019		
[21] Awni et al.	The Effects of Hydrogen Iodide Back Surface Treatment on CdTe Solar Cells	Solar RRL
[22] Paul et al.	Buffer/absorber interface recombination reduction and improvement of back-contact barrier height in CdTe solar cells	Thin Solid Films
[14] Swartz et al.	Absolute photoluminescence intensity in thin film solar cells	J. Appl. Phys.
[23] Swartz et al.	Measurement of band offsets and shunt resistance in CdTe solar cells through temperature and intensity dependence of open circuit voltage and photoluminescence	Solar Energy
[24] Li et al.	Eliminating S-Kink To Maximize the Performance of MgZnO/CdTe Solar Cells	ACS Appl. Energy Mater.
In Progress		
Swartz et al.	Measurement of shunt resistance and conduction band offset in $CuIn_{1-x}Ga_xSe_2$ solar cells through joint analysis of temperature and intensity dependence of open-circuit voltage and photoluminescence	
Paul et al.	Effects of Post-Deposition $CdCl_2$ Annealing on Electronic Properties of CdTe Solar Cells	

Conference Presentations and Papers

I. Gulyas. I. Repins, and J. V. Li	Electrical Characterization of Carrier Transport Properties of CZTSe Solar Cells	IEEE 44th PVSC	Oct, 2016
Craig Swartz, Sanjoy Paul, Sandeep Sohal, Mark Holtz, Yanfa Yan, Lorelle Mansfield, and Jian V. Li	Characterizing recombination using the temperature and excitation dependence of open-circuit voltage and photoluminescence	IEEE 44th PVSC	June, 2017
Sanjoy Paul, Roberto Lopez, Md. Dalim Mia, Craig H. Swartz, and Jian V. Li	A Simulation Study on Radiative Recombination Analysis in CIGS Solar Cells	IEEE 44th PVSC	June, 2017
Corey R. Grice, Jian Li and Yanfa Yan	Close-Space Sublimated CdTe Solar Cells with Co-Sputtered CdS_xSe_{1-x} Alloy Window Layers	IEEE 44th PVSC	June, 2017
Corey R. Grice, Jian Li and Yanfa Yan	Characterization of Single-Source Deposited Close-Space Sublimation $CdTe_xSe_{1-x}$ Thin Film Solar Cells	IEEE 44th PVSC	June, 2017
Roberto Lopez, Sanjoy Paul, Ingrid Repins, and Jian V. Li	Electrical Characterization of carrier transport properties in a CIGS solar cell	IEEE 44th PVSC	June, 2017
Texas State, Univ. Toledo, NREL teams	Crosscutting Recombination Metrology for Expediting Voc Engineering	SETO Portfolio Review	Feb, 2018

Acknowledgments

The Texas State University Principal Investigator acknowledges the full PI Team. Dr. Jian V. Li, Professor, National Cheng Kung University. Dr. Yanfa Yan, Professor, University of Toledo. Dr. Lorelle Mansfield, Scientist, National Renewable Energy Laboratory. The PI Team acknowledges the postdoctoral researchers and students who dedicated formative portions of their careers to this project. The PI Team would also like to acknowledge support of the Program Manager Dr. Brion Bob during the full term of this project.

References

[1] S. Grover, J. V. Li, D. L. Young, P. Stradins, and H. M. Branz, "Reformulation of solar cell physics to facilitate experimental separation of recombination pathways," *Applied Physics Letters,* vol. 103, no. 9, p. 093502, 2013.

[2] J. V. Li, S. Grover, M. A. Contreras, K. Ramanathan, D. Kuciauskas, and R. Noufi, "A recombination analysis of Cu(In,Ga)Se2 solar cells with low and high Ga compositions," *Solar Energy Materials and Solar Cells,* vol. 124, pp. 143-149, 2014/05/01/ 2014.

[3] T. Kato, J. Wu, Y. Hirai, H. Sugimoto, and V. Bermudez, "Record Efficiency for Thin-Film Polycrystalline Solar Cells Up to 22.9% Achieved by Cs-Treated Cu(In,Ga)(Se,S)2," *IEEE Journal of Photovoltaics,* vol. 9, no. 1, pp. 325-330, 2019.

[4] J. Chantana, T. Kato, H. Sugimoto, and T. Minemoto, "Investigation of correlation between open-circuit voltage deficit and carrier recombination rates in Cu(In,Ga)(S,Se)2-based thin-film solar cells," *Applied Physics Letters,* vol. 112, no. 15, p. 151601, 2018.

[5] J. Chantana, T. Kato, H. Sugimoto, and T. Minemoto, "Structures of Cu(In,Ga)(S,Se)2 solar cells for minimizing open-circuit voltage deficit: Investigation of carrier recombination rates," *Progress in Photovoltaics: Research and Applications,* vol. 27, no. 7, pp. 630-639, 2019.

[6] T. Kato *et al.*, "Enhanced Efficiency of Cd-Free Cu(In,Ga)(Se,S)2 Minimodule Via (Zn,Mg)O Second Buffer Layer and Alkali Metal Post-Treatment," *IEEE Journal of Photovoltaics,* vol. 7, no. 6, pp. 1773-1780, 2017.

[7] K. F. Tai, R. Kamada, T. Yagioka, T. Kato, and H. Sugimoto, "From 20.9 to 22.3% Cu(In,Ga)(S,Se)2solar cell: Reduced recombination rate at the heterojunction and the depletion region due to K-treatment," *Japanese Journal of Applied Physics,* vol. 56, no. 8S2, p. 08MC03, 2017/07/06 2017.

[8] H. Guthrey, J. Moseley, J. Nishinaga, H. Shibata, H. Takahashi, and M. Al-Jassim, "Spatially Resolved Recombination Analysis of CuInxGa1-xSe2Absorbers With Alkali Postdeposition Treatments," *IEEE Journal of Photovoltaics,* vol. 8, no. 6, pp. 1833-1840, 2018.

[9] S. Kim *et al.*, "Reduced recombination in a surface-sulfurized Cu(InGa)Se2 thin-film solar cell," *Japanese Journal of Applied Physics,* vol. 57, no. 5, p. 055701, 2018/03/29 2018.

[10] M. Richter *et al.*, "Comprehensive simulation model for Cu(In,Ga)(Se,S)2 solar cells," *Solar Energy Materials and Solar Cells,* vol. 132, pp. 162-171, 2015/01/01/ 2015.

[11] J. Schoneberg, J. Ohland, P. Eraerds, T. Dalibor, J. Parisi, and M. Richter, "Accessing the band alignment in high efficiency Cu(In,Ga)(Se,S)2 (CIGSSe) solar cells with an InxSy:Na buffer based on temperature dependent measurements and simulations," *Journal of Applied Physics,* vol. 123, no. 15, p. 155701, 2018.

[12] N. M. Mangan *et al.*, "Framework to predict optimal buffer layer pairing for thin film solar cell absorbers: A case study for tin sulfide/zinc oxysulfide," *Journal of Applied Physics,* vol. 118, no. 11, p. 115102, 2015.

[13] X. Sun, T. Silverman, R. Garris, C. Deline, and M. A. Alam, "An Illumination- and Temperature-Dependent Analytical Model for Copper Indium Gallium Diselenide (CIGS) Solar Cells," *IEEE Journal of Photovoltaics,* vol. 6, no. 5, pp. 1298-1307, 2016.

[14] C. H. Swartz, S. Paul, L. M. Mansfield, and M. W. Holtz, "Absolute photoluminescence intensity in thin film solar cells," *Journal of Applied Physics,* vol. 125, no. 5, p. 053103, 2019.

[15] R. E. Brandt, N. M. Mangan, J. V. Li, Y. S. Lee, and T. Buonassisi, "Determining interface properties limiting open-circuit voltage in heterojunction solar cells," *Journal of Applied Physics,* vol. 121, no. 18, p. 185301, 2017.

[16] S. Sohal *et al.*, "Carrier Lifetimes of Iodine-Doped CdMgTe/CdSeTe Double Heterostructures Grown by Molecular Beam Epitaxy," *Journal of Electronic Materials,* journal article June 21 2017.

[17] J. V. Li, L. M. Mansfield, B. Egaas, and K. Ramanathan, "Electrical properties of CdS/Cu(In,Ga)Se2 interface," *Japanese Journal of Applied Physics,* vol. 57, no. 8, p. 085701, 2018/06/27 2018.

[18] S. Sohal, M. Edirisooriya, T. Myers, and M. Holtz, "Investigation of cadmium telluride grown by molecular-beam epitaxy using micro-Raman spectroscopy below and above the laser damage threshold," *Journal of Vacuum Science & Technology B,* vol. 36, no. 5, p. 052905, 2018.

[19] M. D. Mia *et al.*, "Electrical and optical characterization of CdTe solar cells with CdS and CdSe buffers—A comparative study," *Journal of Vacuum Science & Technology B,* vol. 36, no. 5, p. 052904, 2018.

[20] S. Paul, R. Lopez, I. L. Repins, and J. V. Li, "Study of charge transport properties in a ZnO/CdS/Cu(In,Ga)Se2 solar cell via admittance spectroscopy," *Journal of Vacuum Science & Technology B,* vol. 36, no. 2, p. 022904, 2018.

[21] R. A. Awni *et al.*, "The Effects of Hydrogen Iodide Back Surface Treatment on CdTe Solar Cells," *Solar RRL,* vol. 3, no. 3, p. 1800304, 2019.

[22] S. Paul *et al.*, "Buffer/absorber interface recombination reduction and improvement of back-contact barrier height in CdTe solar cells," *Thin Solid Films,* vol. 685, pp. 385-392, 2019/09/01/ 2019.

[23] C. H. Swartz *et al.*, "Measurement of band offsets and shunt resistance in CdTe solar cells through temperature and intensity dependence of open circuit voltage and photoluminescence," *Solar Energy,* vol. 189, pp. 389-397, 2019/09/01/ 2019.

[24] D.-B. Li *et al.*, "Eliminating S-Kink To Maximize the Performance of MgZnO/CdTe Solar Cells," *ACS Applied Energy Materials,* vol. 2, no. 4, pp. 2896-2903, 2019/04/22 2019.

[25] G. T. Koishiyev, J. R. Sites, S. S. Kulkarni, and N. G. Dhere, "Determination of back contact barrier height in Cu(In,Ga)(Se,S)2 and CdTe solar cells," in *2008 33rd IEEE Photovoltaic Specialists Conference*, 2008, pp. 1-3.

[26] S. H. Demtsu, D. S. Albin, J. W. Pankow, and A. Davies, "Stability study of CdS/CdTe solar cells made with Ag and Ni back-contacts," (in English), *Solar Energy Materials and Solar Cells,* Article vol. 90, no. 17, pp. 2934-2943, 2006.

[27] J. Pan, M. Gloeckler, and J. R. Sites, "Hole current impedance and electron current enhancement by back-contact barriers in CdTe thin film solar cells," *Journal of Applied Physics,* vol. 100, no. 12, p. 124505, 2006.

[28] J. Li, H. Wei, Y. Li, Q. Li, and N. Li, "Identification of a suitable endogenous control gene in porcine blastocysts for use in quantitative PCR analysis of microRNAs," *Science China Life Sciences,* journal article vol. 55, no. 2, pp. 126-131, February 01 2012.

[29] A. T. Marin, K. P. Musselman, and J. L. MacManus-Driscoll, "Accurate determination of interface trap state parameters by admittance spectroscopy in

the presence of a Schottky barrier contact: Application to ZnO-based solar cells," *Journal of Applied Physics,* vol. 113, no. 14, p. 144502, 2013.

[30] J. V. Li, S. W. Johnston, X. Li, D. S. Albin, T. A. Gessert, and D. H. Levi, "Discussion of some “trap signatures” observed by admittance spectroscopy in CdTe thin-film solar cells," *Journal of Applied Physics,* vol. 108, no. 6, p. 064501, 2010.

[31] J. Lauwaert *et al.*, "Assignment of capacitance spectroscopy signals of CIGS solar cells to effects of non-ohmic contacts," (in English), *Solar Energy Materials and Solar Cells,* Article vol. 112, pp. 78-83, 2013.

[32] W. Jaegermann, A. Klein, and T. Mayer, "Interface Engineering of Inorganic Thin-Film Solar Cells – Materials-Science Challenges for Advanced Physical Concepts," *Advanced Materials,* vol. 21, no. 42, pp. 4196-4206, 2009.

[33] T. Wang *et al.*, "Control of Cu doping and CdTe/Te interface modification for CdTe solar cells," (in English), *Materials Science in Semiconductor Processing,* Article vol. 72, pp. 46-51, 2017.

[34] T. Song, A. Moore, and J. R. Sites, "Te Layer to Reduce the CdTe Back-Contact Barrier," *IEEE Journal of Photovoltaics,* vol. 8, no. 1, pp. 293-298, 2018.

[35] W. Xia *et al.*, "Te/Cu bi-layer: A low-resistance back contact buffer for thin film CdS/CdTe solar cells," (in English), *Solar Energy Materials and Solar Cells,* Article vol. 128, pp. 411-420, 2014.

[36] B. A. Korevaar, R. Shuba, A. Yakimov, H. Cao, J. C. Rojo, and T. R. Tolliver, "Initial and degraded performance of thin film CdTe solar cell devices as a function of copper at the back contact," (in English), *Thin Solid Films,* Conference Paper vol. 519, no. 21, pp. 7160-7163, 2011.

[37] M. M. Tessema and D. M. Giolando, "Pinhole treatment of a CdTe photovoltaic device by electrochemical polymerization technique," (in English), *Solar Energy Materials and Solar Cells,* Article vol. 107, pp. 9-12, 2012.

[38] J. D. Major *et al.*, "P3HT as a pinhole blocking back contact for CdTe thin film solar cells," (in English), *Solar Energy Materials and Solar Cells,* Article vol. 172, pp. 1-10, 2017.

[39] S. Dongaonkar *et al.*, "Universality of non-Ohmic shunt leakage in thin-film solar cells," *Journal of Applied Physics,* vol. 108, no. 12, p. 124509, 2010.

[40] D. S. H. Chan, J. R. Phillips, and J. C. H. Phang, "A comparative study of extraction methods for solar cell model parameters," (in English), *Solid State Electronics,* Article vol. 29, no. 3, pp. 329-337, 1986.

[41] A. R. Jordehi, "Parameter estimation of solar photovoltaic (PV) cells: A review," (in English), *Renewable and Sustainable Energy Reviews,* Review vol. 61, pp. 354-371, 2016.

[42] F. Khan, S. N. Singh, and M. Husain, "Determination of the diode parameters of a-Si and CdTe solar modules using variation of the intensity of illumination: An application," (in English), *Solar Energy,* Article vol. 85, no. 9, pp. 2288-2294, 2011.

[43] M. Turek, "Current and illumination dependent series resistance of solar cells," *Journal of Applied Physics,* vol. 115, no. 14, p. 144503, 2014.

[44] S. S. Hegedus and W. N. Shafarman, "Thin-film solar cells: Device measurements and analysis," (in English), *Progress in Photovoltaics: Research and Applications,* Article vol. 12, no. 2-3, pp. 155-176, 2004.

[45] S. Fiat, Z. Merdan, and T. Memmedli, "Current-conduction mechanisms in Au/n-CdTe Schottky solar cells in the wide temperature range," (in English), *Physica B: Condensed Matter,* Article vol. 407, no. 13, pp. 2560-2565, 2012.

[46] M. Gloeckler, A. L. Fahrenbruch, and J. R. Sites, "Numerical modeling of CIGS and CdTe solar cells: Setting the baseline," 2003, vol. A, pp. 491-494.

[47] M. G. Helander, M. T. Greiner, Z. B. Wang, W. M. Tang, and Z. H. Lu, "Work function of fluorine doped tin oxide," *Journal of Vacuum Science & Technology A,* vol. 29, no. 1, p. 011019, 2011.

[48] A. Klein, "Energy band alignment in chalcogenide thin film solar cells from photoelectron spectroscopy," *Journal of Physics: Condensed Matter,* vol. 27, no. 13, p. 134201, 2015/03/13 2015.

[49] T. I. Seidman and S. C. Choo, "Iterative scheme for computer simulation of semiconductor devices," (in English), *Solid State Electronics,* Article vol. 15, no. 11, pp. 1229-1235, 1972.

[50] R. Storn and K. Price, "Differential Evolution - A Simple and Efficient Heuristic for Global Optimization over Continuous Spaces," (in English), *Journal of Global Optimization,* Article vol. 11, no. 4, pp. 341-359, 1997.

[51] A. Halverson, A. Yakimov, A. Vert, O. Sulima, and B. Korevaar, "Side-by-side characterization of non-optimized and optimized CdS/CdTe solar cells on commercial transparent conductive oxide/glass," (in English), *Thin Solid Films,* Conference Paper vol. 535, no. 1, pp. 249-252, 2013.

[52] T. Ott *et al.*, "Verification of phototransistor model for Cu(In,Ga)Se2solar cells," (in English), *Thin Solid Films,* Conference Paper vol. 582, pp. 392-396, 2015.

[53] C. M. Proctor and T.-Q. Nguyen, "Effect of leakage current and shunt resistance on the light intensity dependence of organic solar cells," *Applied Physics Letters,* vol. 106, no. 8, p. 083301, 2015.

[54] T. Song, A. Kanevce, and J. R. Sites, "Emitter/absorber interface of CdTe solar cells," *Journal of Applied Physics,* vol. 119, no. 23, p. 233104, 2016.

[55] G. Sozzi, F. Troni, and R. Menozzi, "On the combined effects of window/buffer and buffer/absorber conduction-band offsets, buffer thickness and doping on thin-film solar cell performance," (in English), *Solar Energy Materials and Solar Cells,* Article vol. 121, pp. 126-136, 2014.

[56] C. Schubbert *et al.*, "Anomalous temperature dependence of the open-circuit voltage of InS-buffered Cu(In,Ga)(Se,S) solar cells simulated in broad temperature range," *physica status solidi (a),* vol. 213, no. 5, pp. 1276-1283, 2016.

[57] J. F. L. Salas, M. Richter, J. Parisi, and S. J. Heise, "Simulation of photoluminescence lifetime and open-circuit voltage in Cu(In,Ga)Se2 thin film solar cells," *Journal of Applied Physics,* vol. 122, no. 20, p. 203103, 2017.

[58] J. M. Kephart, R. M. Geisthardt, and W. S. Sampath, "Optimization of CdTe thin-film solar cell efficiency using a sputtered, oxygenated CdS window layer," *Progress in Photovoltaics: Research and Applications,* vol. 23, no. 11, pp. 1484-1492, 2015.

[59] D. M. Meysing *et al.*, "Evolution of oxygenated cadmium sulfide (CdS:O) during high-temperature CdTe solar cell fabrication," (in English), *Solar Energy Materials and Solar Cells,* Article vol. 157, pp. 276-285, 2016.

[60] J. H. Werner and H. H. Güttler, "Barrier inhomogeneities at Schottky contacts," (in English), *Journal of Applied Physics,* Article vol. 69, no. 3, pp. 1522-1533, 1991.

[61] R. T. Tung, "Electron transport of inhomogeneous Schottky barriers," (in English), *Applied Physics Letters,* Article vol. 58, no. 24, pp. 2821-2823, 1991.

[62] J. Perrenoud *et al.*, "A comprehensive picture of Cu doping in CdTe solar cells," *Journal of Applied Physics,* vol. 114, no. 17, p. 174505, 2013.

[63] C. S. Ruschel, F. P. Gasparin, E. R. Costa, and A. Krenzinger, "Assessment of PV modules shunt resistance dependence on solar irradiance," (in English), *Solar Energy,* Article vol. 133, pp. 35-43, 2016.

[64] A. Bosio *et al.*, "Interface phenomena between CdTe and ZnTe:Cu back contact," (in English), *Solar Energy,* Article vol. 176, pp. 186-193, 2018.

[65] X. Li, K. Shen, Q. Li, Y. Deng, P. Zhu, and D. Wang, "Roll-over behavior in current-voltage curve introduced by an energy barrier at the front contact in thin film CdTe solar cell," (in English), *Solar Energy,* Article vol. 165, pp. 27-34, 2018.

[66] J. V. Li *et al.*, "Theoretical analysis of effects of deep level, back contact, and absorber thickness on capacitance-voltage profiling of CdTe thin-film solar cells," (in English), *Solar Energy Materials and Solar Cells,* Article vol. 100, pp. 126-131, 2012.

[67] I. Rimmaudo *et al.*, "Improved stability of CdTe solar cells by absorber surface etching," (in English), *Solar Energy Materials and Solar Cells,* Article vol. 162, pp. 127-133, 2017.

[68] J. W. Boucher *et al.*, "Optical response of deep defects as revealed by transient photocapacitance and photocurrent spectroscopy in CdTe/CdS solar cells," (in English), *Solar Energy Materials and Solar Cells,* Article vol. 129, pp. 57-63, 2014.

[69] B. Zhang *et al.*, "Phonon blocking by two dimensional electron gas in polar CdTe/PbTe heterojunctions," *Applied Physics Letters,* vol. 104, no. 16, p. 161601, 2014.

[70] M. A. Green *et al.*, "Solar cell efficiency tables (Version 53)," *Progress in Photovoltaics: Research and Applications,* vol. 27, no. 1, pp. 3-12, 2019.

[71] R. L. Garris, S. Johnston, J. V. Li, H. L. Guthrey, K. Ramanathan, and L. M. Mansfield, "Electrical characterization and comparison of CIGS solar cells made with different structures and fabrication techniques," *Solar Energy Materials and Solar Cells,* vol. 174, pp. 77-83, 2018/01/01/ 2018.

[72] L. M. Mansfield *et al.*, "Comparison of CIGS Solar Cells Made With Different Structures and Fabrication Techniques," *IEEE Journal of Photovoltaics,* vol. 7, no. 1, pp. 286-293, 2017.

[73] X. Zhang, M. Kobayashi, and A. Yamada, "Comparison of Ag(In,Ga)Se2/Mo and Cu(In,Ga)Se2/Mo Interfaces in Solar Cells," *ACS Applied Materials & Interfaces,* vol. 9, no. 19, pp. 16215-16220, 2017/05/17 2017.

[74] T. Eisenbarth, T. Unold, R. Caballero, C. A. Kaufmann, and H.-W. Schock, "Interpretation of admittance, capacitance-voltage, and current-voltage

signatures in Cu(In,Ga)Se2 thin film solar cells," *Journal of Applied Physics,* vol. 107, no. 3, p. 034509, 2010.

[75] P. Aryal *et al.*, "Parameterized complex dielectric functions of CuIn1−xGaxSe2: applications in optical characterization of compositional non-uniformities and depth profiles in materials and solar cells," *Progress in Photovoltaics: Research and Applications,* vol. 24, no. 9, pp. 1200-1213, 2016.

[76] B. L. Williams *et al.*, "Identifying parasitic current pathways in CIGS solar cells by modelling dark J–V response," *Progress in Photovoltaics: Research and Applications,* vol. 23, no. 11, pp. 1516-1525, 2015.

[77] A. R. Davies and J. R. Sites, "Effects of non-uniformity on rollover phenomena in CdS/CdTe solar cells," in *2008 33rd IEEE Photovoltaic Specialists Conference*, 2008, pp. 1-3.

[78] T. Song, J. T. McGoffin, and J. R. Sites, "Interface-Barrier-Induced J–V Distortion of CIGS Cells With Sputtered-Deposited Zn(S,O) Window Layers," *IEEE Journal of Photovoltaics,* vol. 4, no. 3, pp. 942-947, 2014.

[79] C.-H. Chung, B. Bob, T.-B. Song, and Y. Yang, "Current–voltage characteristics of fully solution processed high performance CuIn(S,Se)2 solar cells: Crossover and red kink," *Solar Energy Materials and Solar Cells,* vol. 120, pp. 642-646, 2014/01/01/ 2014.

[80] V.-T. Rangel-Kuoppa, M.-d.-L. Albor-Aguilera, C. Hérnandez-Vásquez, J.-M. Flores-Márquez, M.-Á. González-Trujillo, and G.-S. Contreras-Puente, "Shunt resistance and saturation current determination in CdTe and CIGS solar cells. Part 1: a new theoretical procedure and comparison with other methodologies," *Semiconductor Science and Technology,* vol. 33, no. 4, p. 045007, 2018/03/12 2018.

[81] G. Hanna, A. Jasenek, U. Rau, and H. W. Schock, "Influence of the Ga-content on the bulk defect densities of Cu(In,Ga)Se2," *Thin Solid Films,* vol. 387, no. 1, pp. 71-73, 2001/05/29/ 2001.

[82] M. A. Halim *et al.*, "A comparative study on charge carrier recombination across the junction region of Cu2ZnSn(S,Se)4 and Cu(In,Ga)Se2 thin film solar cells," *AIP Advances,* vol. 6, no. 3, p. 035216, 2016.

[83] Y. Wang, T. Muryobayashi, K. Nakada, Z. Li, and A. Yamada, "Correlation between carrier recombination and valence band offset effect of graded Cu(In,Ga)Se2 solar cells," *Solar Energy Materials and Solar Cells,* vol. 201, p. 110070, 2019/10/01/ 2019.

[84] A. Lafuente-Sampietro *et al.*, "Wavelength-dependent J–V characteristics of CuIn1-x Ga x (S,Se)2 solar cells and carrier recombination," *Applied Physics Express,* vol. 12, no. 6, p. 061001, 2019.

[85] J. Chantana *et al.*, "Aging Effect of a Cu(In,Ga)(S,Se)2 Absorber on the Photovoltaic Performance of Its Cd-Free Solar Cell Fabricated by an All-Dry Process: Its Carrier Recombination Analysis," *Advanced Energy Materials,* p. 1902869. 30 October 2019.